buildings

MDPI

Article

Study of the Seismic Behavior of Simplified RCS Joints via Nonlinear Finite Element Analysis

Wei Li [1,2], Zhexiong Wang [1,3], Xuchuan Lin [4], Lianmeng Chen [1,3,*] and Baixi Chen [5,*]

[1] College of Civil Engineering and Architecture, Wenzhou University, Wenzhou 325035, China; weili@wzu.edu.cn (W.L.); zhexiongwang@163.com (Z.W.)
[2] Wenzhou Chengjian Grput Co., Ltd., Wenzhou 325000, China
[3] Key Laboratory of Engineering and Technology for Soft Soil Foundation and Tideland Reclamation of Zhejiang Province, Wenzhou 325035, China
[4] Key Laboratory of Earthquake Engineering and Engineering Vibration, Institute of Engineering Mechanics, China Earthquake Administration, Harbin 150080, China; linxuchuan@iem.ac.cn
[5] Department of Mechanical Engineering, University of Wisconsin-Madison, 1513 University Avenue, Madison, WI 53706, USA
* Correspondence: 00151034@wzu.edu.cn (L.C.); baixi.chen@wisc.edu (B.C.); Tel.: +86-13957790090 (L.C.)

Abstract: Compared to more complex structures, simply configured reinforced concrete column–steel beam (RCS) composite structures have more promising application prospects, especially in regions with moderate–high seismic levels, due to their ease of construction. However, the current understanding of the seismic performance of simplified RCS joints is not sufficient. Validated by experimental results, a nonlinear finite element analysis (FEA) model was developed in this study to reveal the seismic behavior of simplified RCS joints. Six vital design parameters, namely axial load ratio, concrete strength, yield strengths of steel webs and flanges, and diameters of transverse and longitudinal reinforcements, were comprehensively studied. Research has shown that the axial compression ratio has a significant impact on the failure mode and bearing capacity of joints. When the concrete strength increases, the load-bearing capacity of the joints significantly increases, while the brittleness of high-strength concrete leads to a decrease in its deformation capacity. In addition, when the steel beam strength is constant, higher flange and web yield strengths have a limited influence on crack propagation and strain development. The stirrup reinforcement ratio and longitudinal reinforcement ratio play a significant role in inhibiting crack propagation and improving the bearing capacity, respectively. With the help of the numerical results, six theoretical models introduced by national codes and other researchers were compared. Among them, the modified model proposed by Kanno demonstrated the highest accuracy and was the most suitable for simply configured RCS joints.

Keywords: RCS joint; seismic performance; FEA model; capacity evaluation

check for updates

Citation: Li, W.; Wang, Z.; Lin, X.; Chen, L.; Chen, B. Study of the Seismic Behavior of Simplified RCS Joints via Nonlinear Finite Element Analysis. *Buildings* **2023**, *13*, 2718. https://doi.org/10.3390/buildings13112718

Academic Editor: Rajai Zuheir Al-Rousan

Received: 9 October 2023
Revised: 19 October 2023
Accepted: 26 October 2023
Published: 28 October 2023

Copyright: © 2023 by the authors. Licensee MDPI, Basel, Switzerland. This article is an open access article distributed under the terms and conditions of the Creative Commons Attribution (CC BY) license (https://creativecommons.org/licenses/by/4.0/).

1. Introduction

With the advantages of both reinforced concrete (RC) and steel, RC column–steel beam (RCS) structures have a lower structural self-weight and demonstrate outstanding seismic performance. This attractive structure system has been widely used all over the world, especially in high-rise buildings and large-span structures. The connections between the beam and column are usually vulnerable to earthquakes [1,2]. Therefore, as well as being an important structural component, the RCS structure's joints are also the weakest part of the whole system under seismic action, which has been shown by many scholars. The existing strengthening measures for RCS joints mainly include the use of prestressed steel bars, steel cover plates, and other strengthening elements, as well as the use of new materials and energy dissipation components. Changes in joint structure and the use of different materials have varying degrees of impact on the seismic performance and failure mode of joints, hindering improvements to the design and seismic performance of RCS joints [3–10].

Therefore, to ensure the safety and reliability of the RCS structure, it is both theoretically and practically vital to understand the seismic behavior of RCS joints.

Since the mechanical mechanism of the RCS joints is usually influenced by the connection configuration, there have been numerous experimental works focusing on developing effective joints and improving their seismic resistance. Nabati et al. [11] determined the impacts of the form and thickness of web stiffeners on the seismic behavior of RCS joints experimentally and proved that the correct utilization of web stiffeners could enhance the strength, stiffness, and resilience of the joint. Both web stiffeners and flange stiffeners were extensively studied by Le et al. [12] from the aspects of capacity, story drift, and energy dissipation, demonstrating that they have a positive effect on the seismic performance of RCS joints. Herdiansah et al. [13] utilized bearing plates, band plates, and U-shape stirrups to improve the resistance of the RCS joints. Doost and Khaloo [14] employed a steel web panel for joint enhancement and found that it could highly strengthen the joint's shear capacity and control crack development. The effects of transverse stiffeners and beams on the RCS joint capacity were determined by Chen et al. [15] and Cheng et al. [16], respectively. In addition, steel fibers were also considered for RC joint enhancement by Nguye et al. [17].

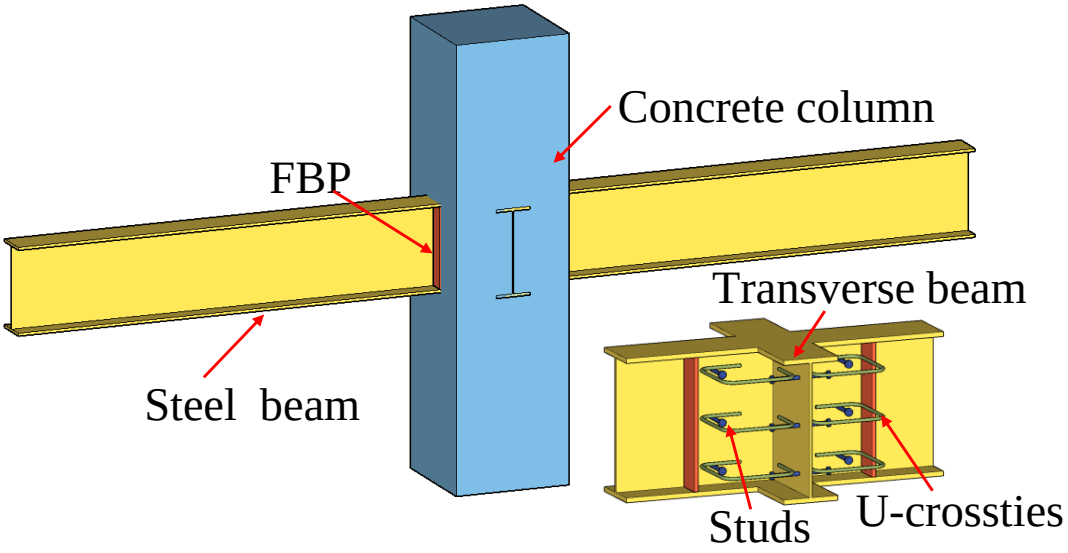
Although the seismic performances of RCS joints can be directly reflected in experiments, the high costs of specimen preparation and testing usually hinder a more comprehensive investigation. Additionally, the stress and strain statuses of RCS joints have been poorly studied in experiments as well. In order to address these issues, a numerical approach is commonly adopted to reveal the mechanisms in RCS joints. With the help of a numerical model, the impacts of various design parameters can be further explored [18–20]. For example, Alizadeh et al. [21] used a numerical model to demonstrate the seismic behavior of RCS joints with an additional bearing plate and a wide face bearing plate. The numerical model developed by Jafari et al. [22] illustrated the benefits of tube plates in RCS joints. Li et al. [23,24] used both experimental and numerical approaches to highlight the superiority of three novel demountable RCS joints.

Most previous experimental and numerical studies attempted to improve the capacity of RCS joints by adopting various complex configurations, some of which are hard to use in practice. Compared to these complex RCS joints with high seismic performances, simply configured RCS joints could be applied in more regions, especially those with moderate–high seismic requirements, due to their ease of construction and lower costs. The vast majority of regions only require moderate–high seismic performance joints, and the application of an RCS joint with a reliable mechanical performance, low cost, and easy construction has broad prospects. Due to limited experimental data, the seismic performance of simplified RCS joints is not fully understood, and due to different strengthening designs and loading methods, these data cannot be directly compared. Therefore, using finite element analysis to study the seismic performance of RCS joints under cyclic loads is a practical and economical option. It is important to comprehensively understand the mechanical mechanism of simply configured RCS joints during earthquakes. In order to reveal the seismic behavior of simply configured RCS joints with a high seismic capacity, in this study, we developed a nonlinear finite element analysis (FEA) model validated by the experimental results to numerically investigate the effects of different design parameters. By means of simulation results, a suitable capacity evaluation method was conceptualized to assist in the design of simply configured RCS joints with a high seismic performance. The results presented in this study could further promote the real-world application of RCS joints.

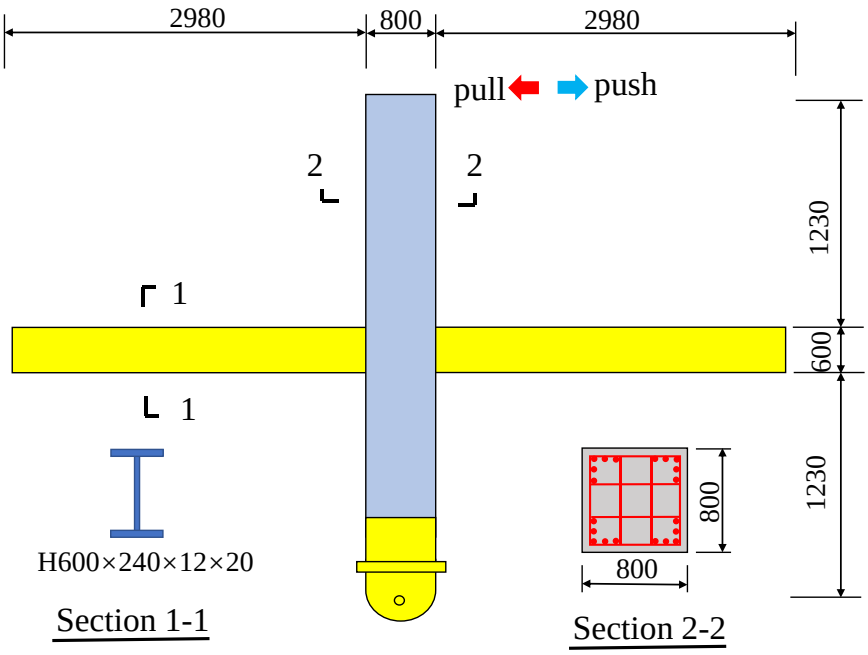
2. Experimental Setup

The experimental study on the RCS joint specimens with the middle seismic design level and the scale of 2/3 in Reference [25] was selected to validate the nonlinear finite element analysis (FEA) model for the numerical investigation. The details of the specimen design and the experimental setup are reproduced below.

A schematic diagram and the dimensions of the RCS structure studied in this paper are shown in Figure 1. Through-beam-type RCS joints were used in this structure which consist of a concrete column, an H-section steel beam, a face bearing plate (FBP), U-crossties, studs, and reinforcements. Four kinds of joint configurations were considered in reference [25], namely TF6, TF16, SF6, and F16, which are detailed in Figure 2. T, S, and F indicate transverse beams, vertical studs, and FBPs, respectively, while the number indicates the thickness of the FBP. For example, TF6 refers to an RCS joint with a transverse beam and a face bearing plate with a thickness of 6 mm. The longitudinal reinforcement and the stirrup adopted here were an SD500 steel bar with a diameter of 29 mm and an SD400 steel bar with a diameter of 13 mm. The arrangement of the steel reinforcements is exhibited in Figure 3. The concrete strength was 40.4 MPa, while the steel properties of the beam, FBP, and reinforcement are presented in Table 1.



(**a**) Three-dimensional (3D) view



(**b**) front view

Figure 1. Schematic diagram of the RCS structure developed in reference [25].

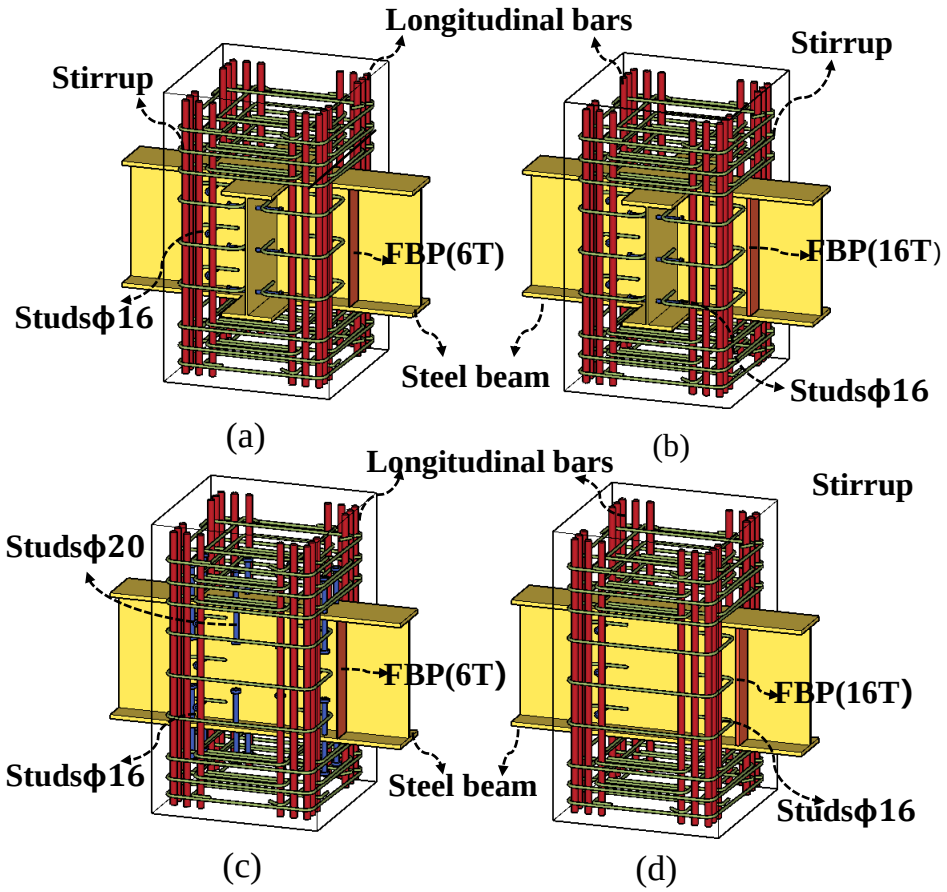


Figure 2. Details of four RCS joint configurations: (**a**) TF6, (**b**) TF16, (**c**) SF6, and (**d**) F16.

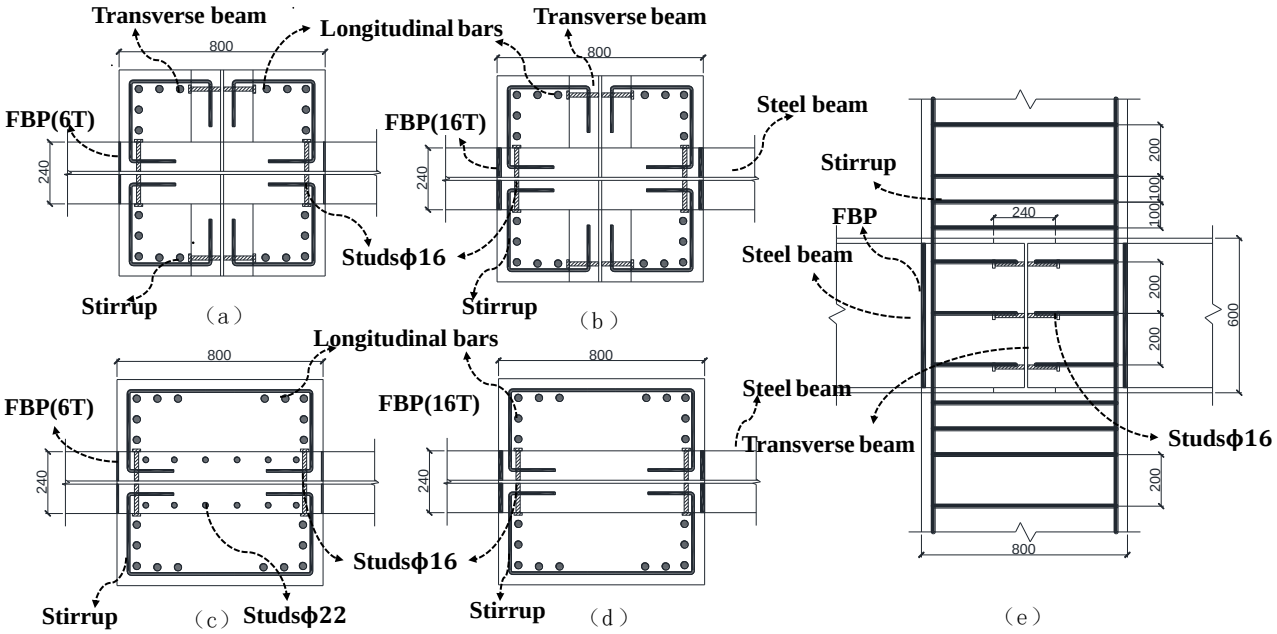


Figure 3. Longitudinal reinforcement arrangement in RCS connection types: (**a**) TF6, (**b**) TF16, (**c**) SF6, and (**d**) F16 and (**e**) the stirrup arrangement [25].

Table 1. Material properties of the steel used for different purposes in RCS joints.

Purpose	Types	Strength Grade	Yield Strength (MPa)	Tensile Strength (MPa)	Elongation (%)
FBP	Thickness of 6 mm	SM490	443	586	30.6
	Thickness of 16 mm	SM490	369	545	33.9
Beam	Web	SM490	386	553	34.4
	Flange	SM490	336	548	20.0
Steel bar	Longitudinal	SD500	539	697	-
	Stirrup	SD400	507	635	-

The loading apparatus for the RCS joints is shown in Figure 4. Two sides of the steel beams and the end of the column were pin supported. The space between the loading center and the column end support was 3060 mm. The loading scheme met the AISC 2010a specifications [26] and is demonstrated in Figure 5. Ten loading levels were used, namely 0.375%, 0.5%, 0.75%, 1%, 1.5%, 2%, 3%, 4%, 5%, and 6%. Six and four cycles were repeated for the first three levels and the fourth level, respectively, while two cycles were conducted for the rest of the loading levels. The horizontal displacement at the top of the column and the vertical displacements at the beam ends were recorded using an LVDT, as indicated in Figure 4. The rebar and steel plate inner joints strains were also detected using strain gages.

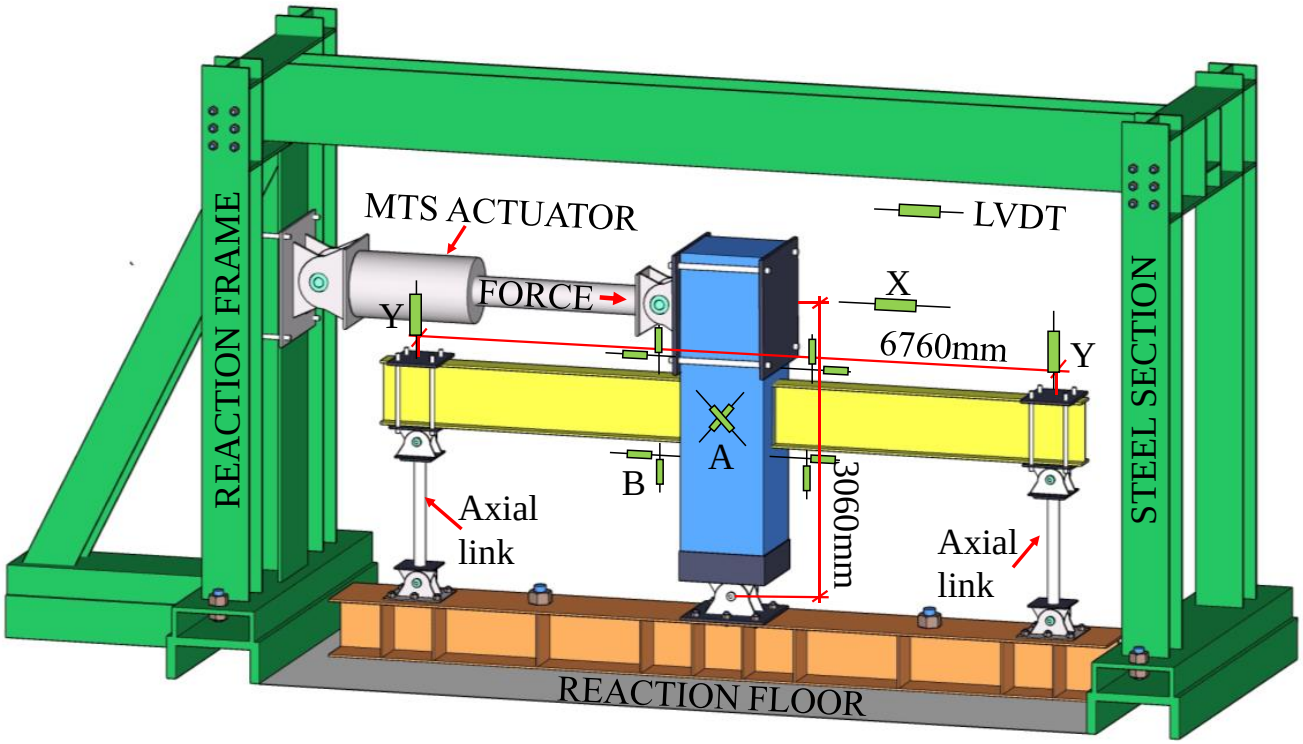


Figure 4. Experimental loading apparatus for the RCS joint.

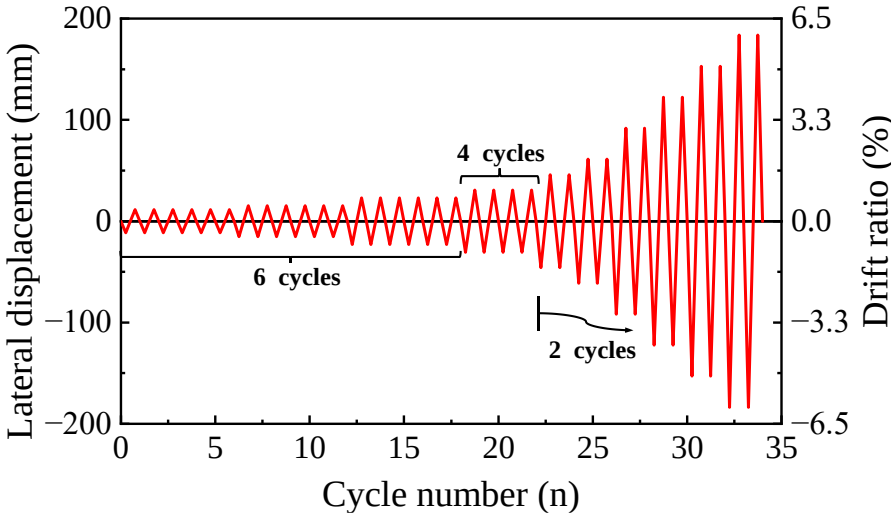


Figure 5. Experimental loading scheme.

3. Numerical Modeling

3.1. Model Setup

The nonlinear FEA model detailed in Figure 6 was developed in Abaqus to numerically model four RCS joints with a moderate–high seismic capacity. The steel beam, the FBP, and the concrete column were modeled by the solid element C3D8R, while the truss element T3D2 was used to describe the reinforcements. The contacts between the concrete and steel components, including the steel beam and rebars, were described by the "embedded" constraint. The stud, FBP, and steel beam were connected by the "tie" constraint to simulate welding. The FEA model's boundary conditions were consistent with the experimental setup. Except for the in-plane rotation, all other degrees of freedom of the column bottom and the beam ends were fixed. For simplicity, the portion of the column above the loading center, that is, 3060 mm above the end of the column, was not modeled here. As indicated by a sensitive study of the mesh size, element sizes of 30 and 50 for the column and steel beam, respectively, were sufficient for both the accuracy requirement and calculation efficiency, and they were used in this study.

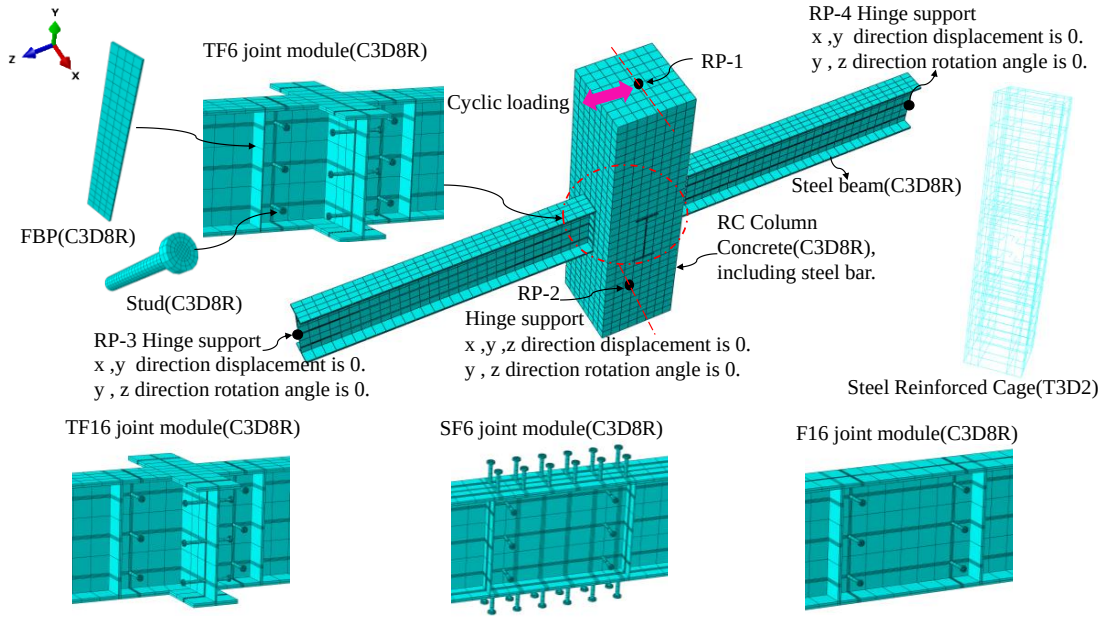


Figure 6. FEA model for four types of RCS joints.

The mean compressive strength of concrete was used to describe the concrete strength in this study. The Poisson ratio and concrete density were set to 0.2 and 2400 kg/m^3, respectively. The steel strengths used are shown in Table 1. The Poisson ratio and density of the concrete were set to 0.3 and 7800 kg/m^3, respectively. The concrete damage plasticity model in ABAQUS was used to model concrete behavior, as shown in Figure 7a. The stress–strain relationship suggested in the Chinese concrete code GB 50010-2010 [27] was used here. Experimental observations of brittle materials, including concrete, indicate that when the load changes from tension to compression, the compressive stiffness recovers with crack closure. In addition, when the load changes from compression to tension, once micro-cracks occur during compression, the stiffness during tension cannot be restored. Thus, we set $w_t = 0$ and $w_c = 1$ to evaluate the stiffness recovery ability [18]. The von Mises plastic model with isotropic strain hardening was used for a fundamental steel bar and steel structure models without considering the equivalent yield plateau. The stress–strain curve is shown in Figure 7b. The analytic form of the bilinear hardening model is presented below:

$$\sigma_s = \begin{cases} E_s\varepsilon_s & \varepsilon \le \varepsilon_y \\ f_y + \alpha E_s(\varepsilon_s - \varepsilon_y) & \varepsilon > \varepsilon_y \end{cases} \quad (1)$$

where σ_s and ε_s are the stress and strain of the steel, respectively; f_y and ε_y are the yield stress and strain, respectively; E_s is the elastic modulus; αE_s is the stiffness at the hardening stage; and α and E_s are recommended to be 0.01 and 200 GPa for steel, respectively [28].

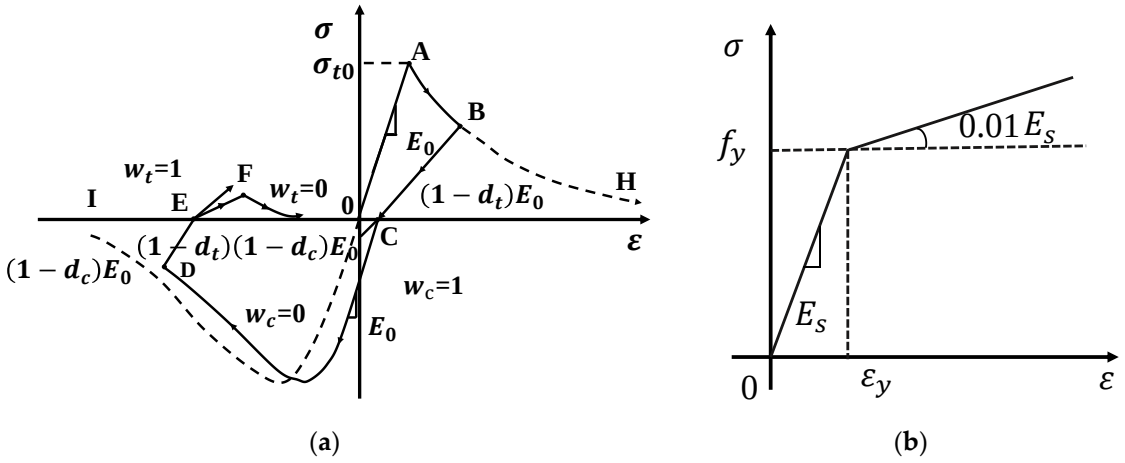


Figure 7. Fundamental behavior of (**a**) steel and (**b**) concrete.

3.2. Model Validation

3.2.1. Hysteresis Curves

The hysteresis curves determined in experiments and by numerical modeling are illustrated in Figure 8. It can be observed that the numerical hysteresis loops were in good agreement with the experimental ones, which validated the feasibility of the FEA model for simulating the seismic performance of RCS joints. All hysteresis loops of RCS joints had a fusiform shape and demonstrated a high energy dissipation capacity. The simulated loads and stiffnesses of the first several loops were slightly higher than the experimental ones. This difference may be attributed to the non-uniform contact between the MTS actuator and the specimens [29]. The pinching effect observed in experiments was not fully reflected in the numerical simulations. Slipping between the steel and concrete led to pinched hysteresis loops during experiments. However, in the FEA model, the steel was embedded into the concrete, and the bond slip behavior between them was hard to model in simulations, resulting in a partial loss of the pinching effect. Additionally, perfect contact between the MTS actuator and the specimens also reduced the pinching effect in the simulations. Without the transverse steel beam, RCS joint specimens SF6 and F16 had a

lower contact area between the steel and concrete, which mitigated the side effects caused by the omission of bond slip behavior. Hence, the simulated and test hysteresis loops of these two specimens were more alike compared to specimens TF6 and TF16.

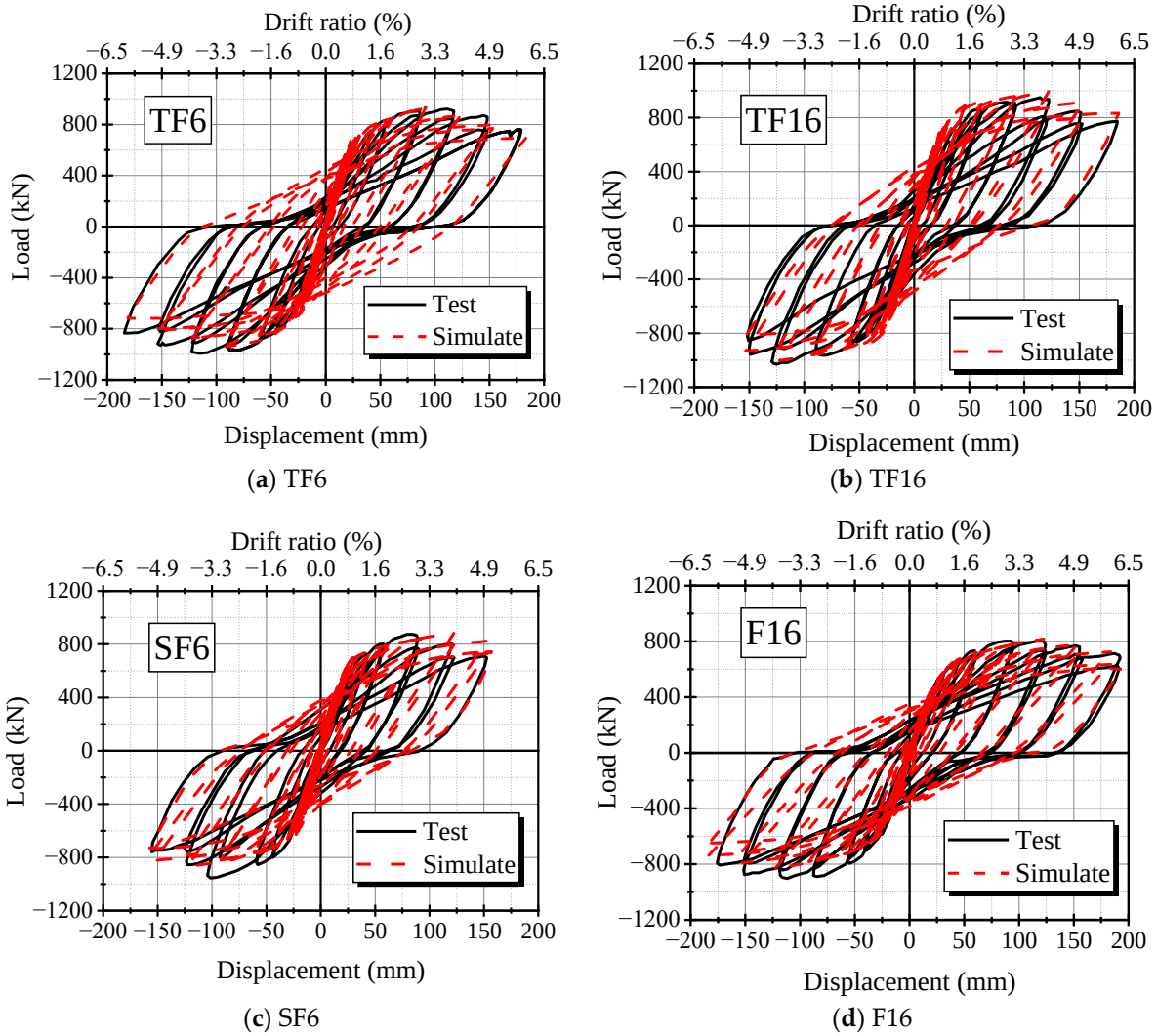


Figure 8. Hysteresis curves of the four RCS joints determined in experimental tests and numerical simulations.

3.2.2. Skeleton Curves and Capacity

Skeleton curves and peak capacities were determined from the hysteresis curves and are exhibited in Figure 9 and Table 2, respectively. The simulated skeleton curves of different RCS joints were consistent with those determined in experiments, and the relative errors of the estimated peak capacity were lower than 3%, which highlights the high accuracy of the developed numerical model. With a thicker FBP, the capacity of specimen TF16 is higher than that of specimen TF6. The existence of a transverse beam increased the contact area between the concrete and the steel beam and improved the integrity of the joints, resulting in higher capacities of specimens TF16 and TF6 compared to the other two. Without additional shear-resistant elements, such as transverse beams and vertical studs, specimen F16 exhibited a lower capacity than the others. However, the lack of additional shear-resistant elements resulted in the formation of a plastic hinge in the joint regions; thus, the skeleton curves of specimen F16 had a gentler descending phase than the others and exhibited better ductility.

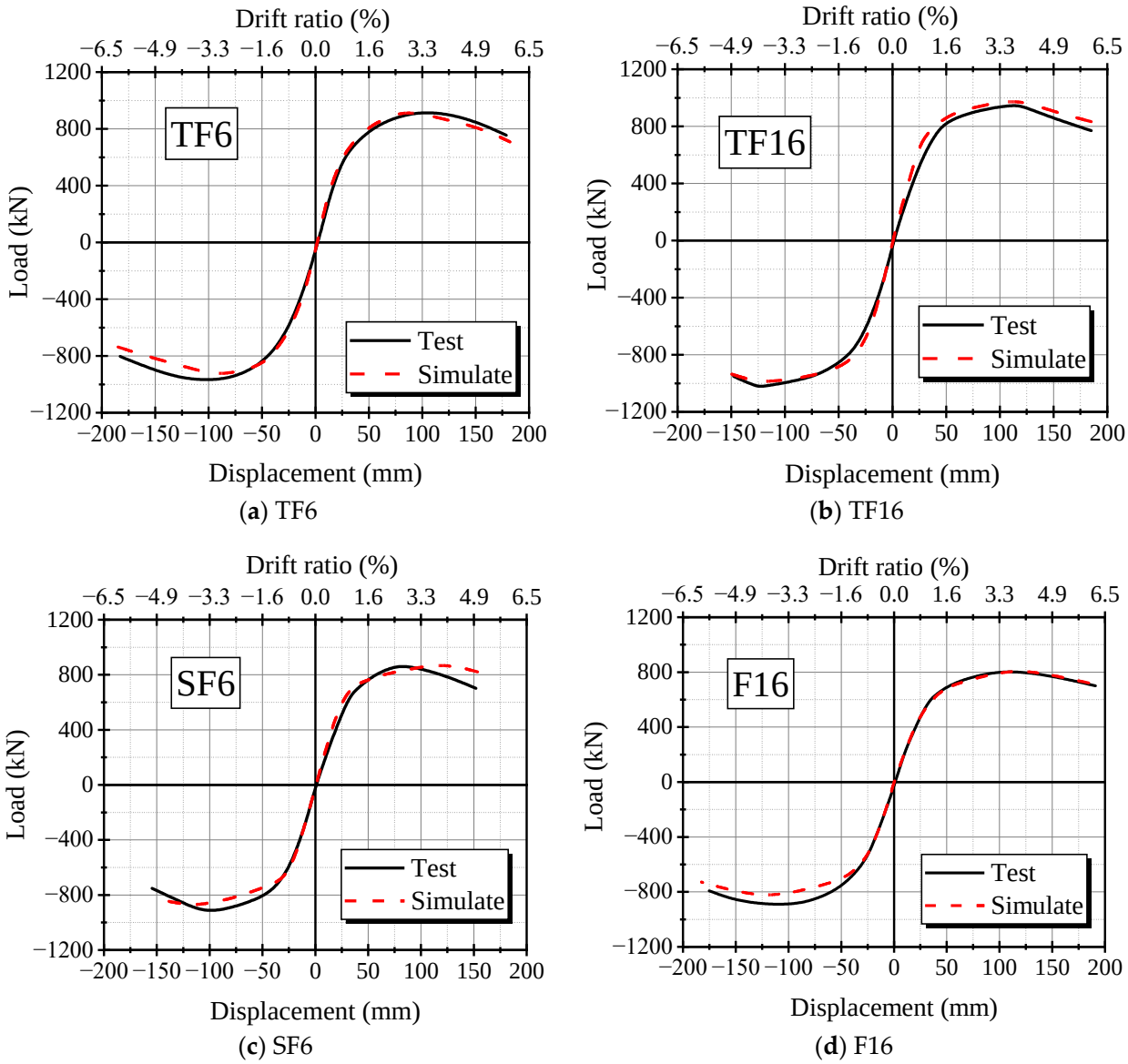


Figure 9. Skeleton curves of four RCS joints determined in experimental tests and numerical simulations.

Table 2. Load capacities of different RCS joint specimens.

Capacity	Specimen			
	TF6	**TF16**	**SF6**	**F16**
Experimental value (kN)	923.00	951.72	868.18	804.17
Numerical value (kN)	919.97	979.31	844.93	816.67
Relative error (%)	0.33	2.90	−2.68	1.55

3.2.3. Crack Patterns

The tension damage patterns of the RCS joints obtained from the FEA model were used to represent the crack pattern of the RCS joints, and they are illustrated in Figure 10 alongside experimental crack patterns. "DAMAGET" in Figure 10 refers to the damage degree under tension force. Its value ranges from 0 to 1, where 0 indicates the concrete is not damaged and 1 indicates the concrete is fully damaged. The damage degree is positively correlated to the crack widths and cracking level and can be used to reflect crack or failure patterns. The cross-oblique crack modes of all specimens observed in the experiments could be clearly observed in the numerical models. The specimens TF6, TF16, and F16 exhibited

a similar level of cracks, while the crack pattern of specimen SF6 was milder than the other three, which was reflected in both experiments and numerical simulations. This is because the vertical studs improved the load transmission and the coupling between the steel beam and the concrete in the joint region. Consistent crack patterns between experiments and numerical simulations indicate the validity of the FEA models.

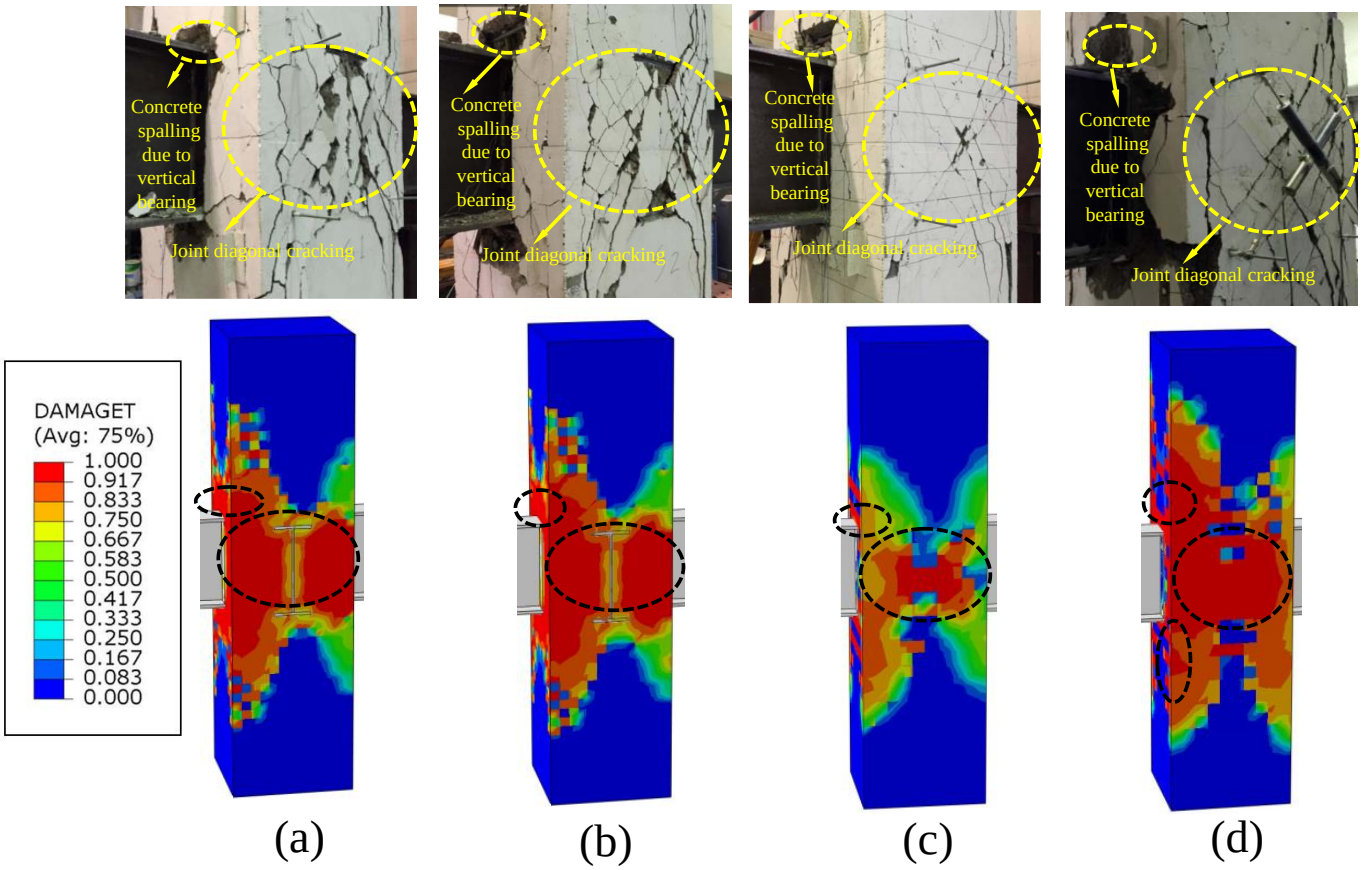


Figure 10. Crack patterns of the specimens (**a**) TF6, (**b**) TF16, (**c**) SF6, and (**d**) F16 determined in experiments and numerical simulations.

3.3. Steel Stress Development in RCS Joints

The four kinds of RCS joint specimens exhibited similar crack modes and hysteresis loops. Therefore, without a loss of generality, the numerical model of the TF6 specimen was adopted to investigate the stress development in the steel beam in the concrete column, which is hard to measure in experiments. Steel stresses at different drift ratios are visualized in Figure 11. The connection between the beam flange at the tension side and the FBP first failed at a drift of 2.0%. This indicates that both the joint and beam failed under seismic load and the developed RCS joint exhibited a hybrid joint–beam failure mode. As the story drift rose, the concrete in the RCS joint core suffered shear deformation, which increased the stress of the steel web in the concrete and made the steel web fail starting from the inner part to the outer part. Surrounded by the concrete, the edge of the FBP exhibited a higher stress than the center and failed first.

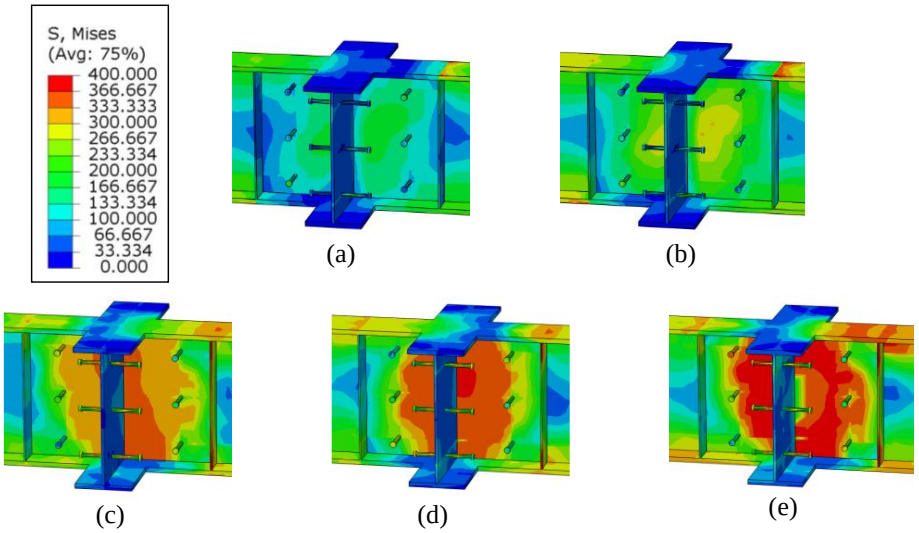


Figure 11. Stress development in the RCS joint steel beam of the TF6 specimen at drifts of (**a**) 1.5%, (**b**) 2.0%, (**c**) 4.0%, (**d**) 5.0%, and (**e**) 6.0%.

4. Parametric Studies

By means of the validated FEA model, parametric studies were conducted to further reveal the mechanism of the RCS joint under seismic action. The influences of six key design parameters, namely the axial load ratio, concrete strength, steel strength, and reinforcement diameter, were investigated. The TF6 specimen was selected as the benchmark, and the seismic performance of the RCS joints was evaluated using a series of measures, including skeleton curves, load capacities, ductility, energy dissipation, and concrete damage modes. The scheme of the parametric studies is shown in Table 3.

Table 3. Scheme of the parametric studies.

Parameters	Specimen No.	Concrete Strength (MPa)	Axial Load Ratio (%)	Yield Strength (MPa)		Reinforcement Diameter (mm)	
				Flange	Web	Transverse	Longitudinal
Benchmark	RCS0	40.4	0	336	386	13	29
Axial load ratio	RCS1	40.4	10	336	386	13	29
	RCS2	40.4	20	336	386	13	29
	RCS3	40.4	30	336	386	13	29
	RCS4	40.4	40	336	386	13	29
	RCS5	40.4	50	336	386	13	29
Concrete strength	RCS6	30	0	336	386	13	29
	RCS7	60	0	336	386	13	29
	RCS8	70	0	336	386	13	29
Steel flange strength	RCS9	40.4	0	235	386	13	29
	RCS10	40.4	0	420	386	13	29
	RCS11	40.4	0	460	386	13	29
Steel web strength	RCS12	40.4	0	336	235	13	29
	RCS13	40.4	0	336	420	13	29
	RCS14	40.4	0	336	460	13	29
Transverse reinforcement diameter	RCS15	40.4	0	336	386	4	29
	RCS16	40.4	0	336	386	8	29
	RCS17	40.4	0	336	386	18	29
Longitudinal reinforcement diameter	RCS18	40.4	0	336	386	13	12
	RCS19	40.4	0	336	386	13	16
	RCS20	40.4	0	336	386	13	20

4.1. Effect of Axial Load Ratio

The axial compressive load is a key factor for evaluating the seismic performance of column beam joints [30]. Figure 12 exhibits the skeleton curves, load capacity, ductility, and energy dissipation of the joints. It can be observed that the elastic stages of all skeleton curves coincided with each other and demonstrated a similar stiffness regardless of the axial load ratio. The increased axial load ratio significantly increased the joint capacity as the axial load enhanced the constraint effect and the contact between steel and concrete and prevented tensile crack development in the concrete to some extent. In addition, the axial load limited the joint's deformation ability, which also worsened the ductility of the RCS joints. The ductility coefficient dropped by 16.45% at the axial load ratio of 50%, as shown in Figure 12b,c. It could be observed in Figure 12d that specimens with different axial load ratios had similar cumulative energy dissipation curve trends, and those with a lower axial load could dissipate more energy. This positive effect may be attributed to the fact that a lower axial load has a fuller and more stable hysteresis loop. When the axial load ratio was over 30%, further increases in the axial load brought minor benefits, as the high axial compression load induced additional compressive cracks. Figure 13 demonstrates the tensile and compressive crack patterns determined using numerical modeling. Cross-tensile cracks could be effectively reduced by increasing the axial load, while compressive crack patterns were slightly improved by a low-level axial load. When the axial load was over 30%, further increases in the axial load introduced additional compressive cracks and gradually enlarged the compressive crack area.

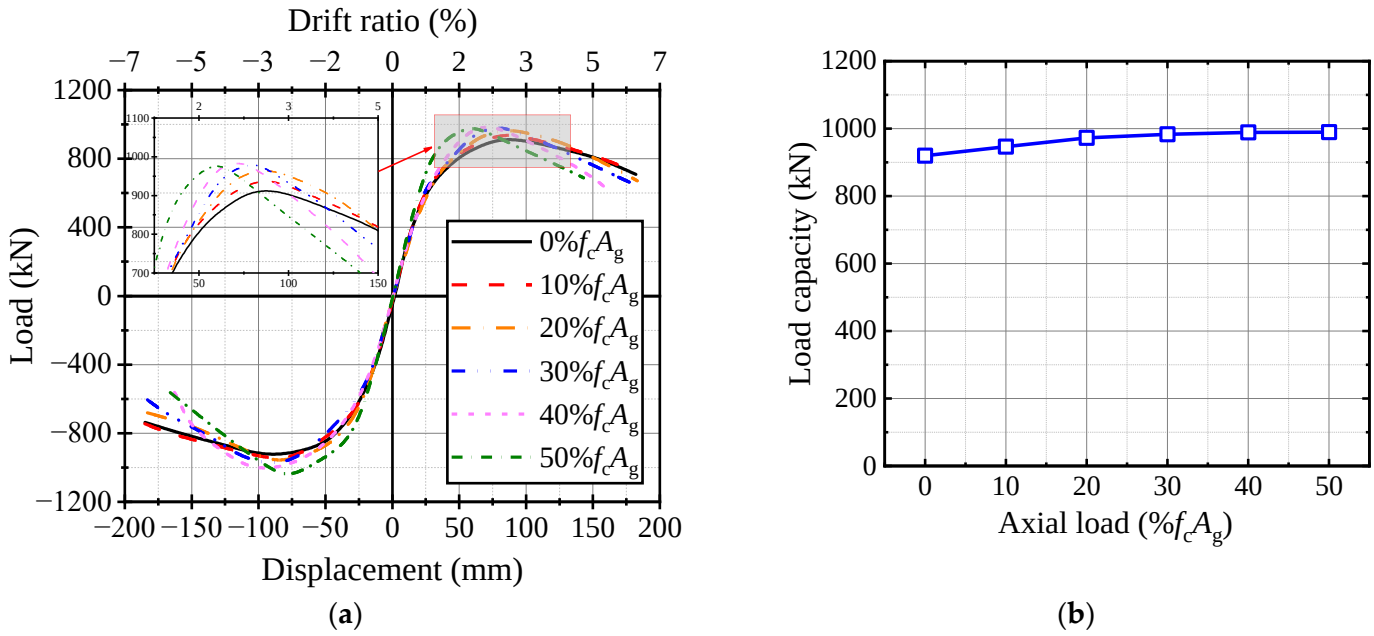
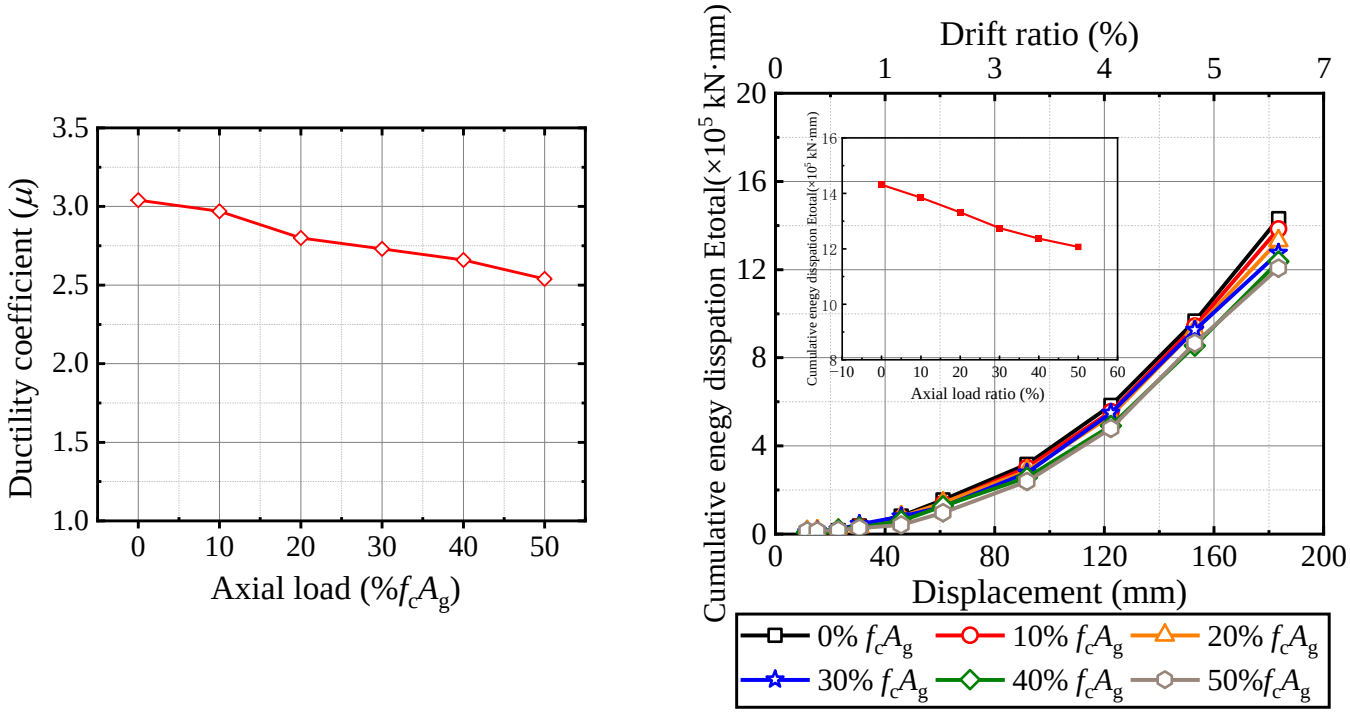
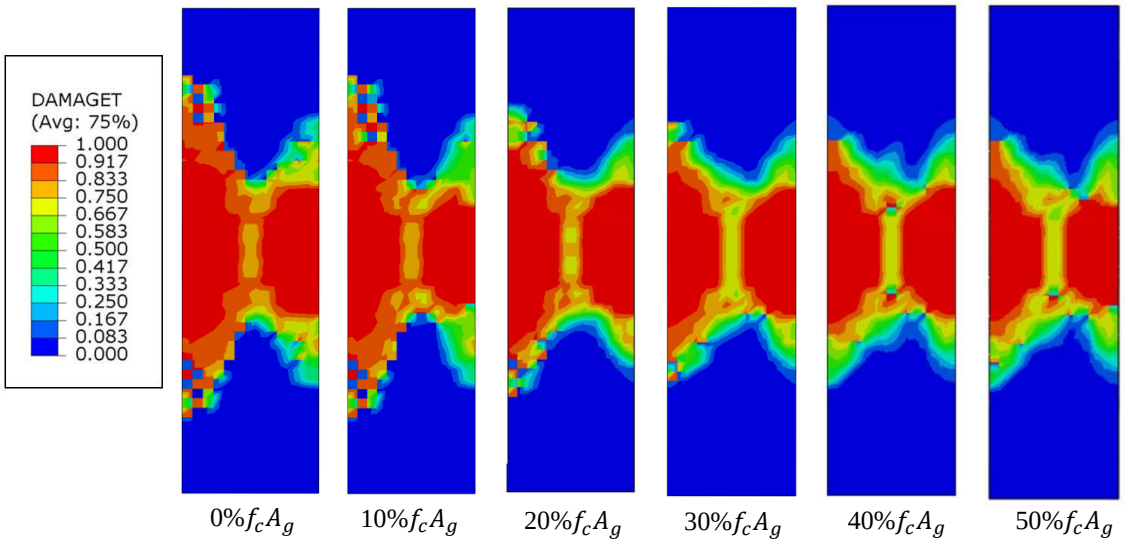


Figure 12. *Cont.*



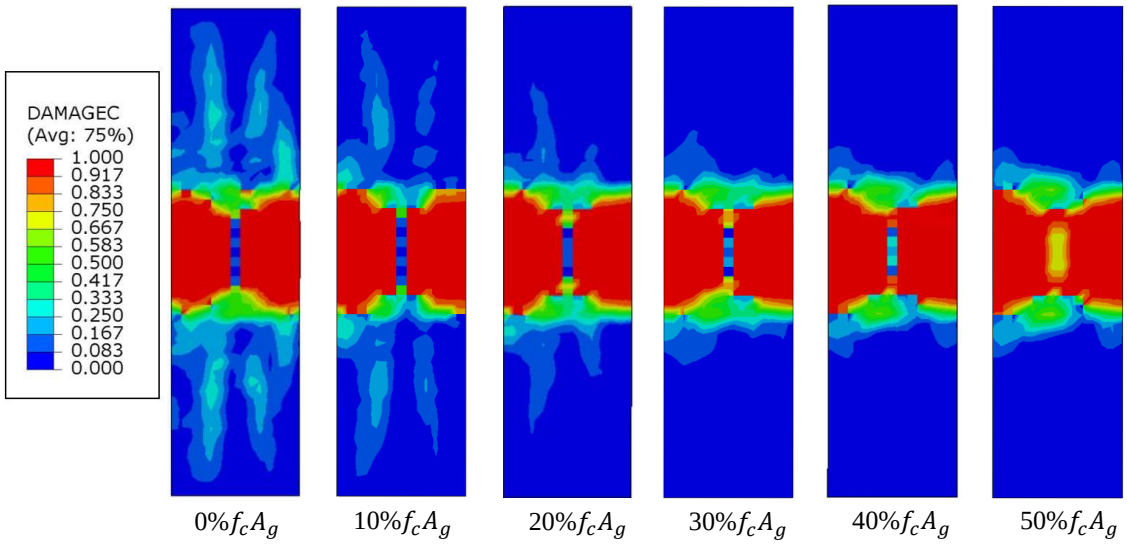
(**c**) (**d**)

Figure 12. Influence of the axial load ratio on (**a**) skeleton curves, (**b**) load capacity, (**c**) ductility coefficient, and (**d**) cumulative energy dissipation.



(**a**) Tensile damage status

Figure 13. *Cont.*



(**b**) Compressive damage status

Figure 13. (**a**) Tensile and (**b**) compressive damage status at different axial load ratios when the story drift reached 6%.

4.2. Effect of Concrete Strength

The skeleton curves and load capacities of RCS joints at different concrete strengths are exhibited in Figure 14a,b. With an increase in concrete strength, the skeleton curve gradually went up, which resulted in a higher stiffness and load capacity. It could be noted in Figure 14 that the load capacity increased by 15.6% when the strength increased from 30 to 70 MPa. However, the low ductility of the high-strength concrete weakened the ductility of the joints by 7.6%, as indicated in Figure 14c. The cumulative energy dissipation in the RCS joint is demonstrated in Figure 14d. When the story drift was lower than 1%, the energy dissipation was barely influenced by the concrete strength. With a rise in story drift, the concrete strength had a positive effect due to an increase in capacity. The cumulative energy dissipation improved by 16.39% when 70 MPa concrete was used. Figure 15 illustrates the concrete damage status at different concrete strengths. The utilization of high-strength concrete could suppress cross-tensile crack formation to some extent. With an increase in the concrete strength, the compressive damage was mainly concentrated in the joint core region and damage to other parts was mitigated, as noted in Figure 15b.

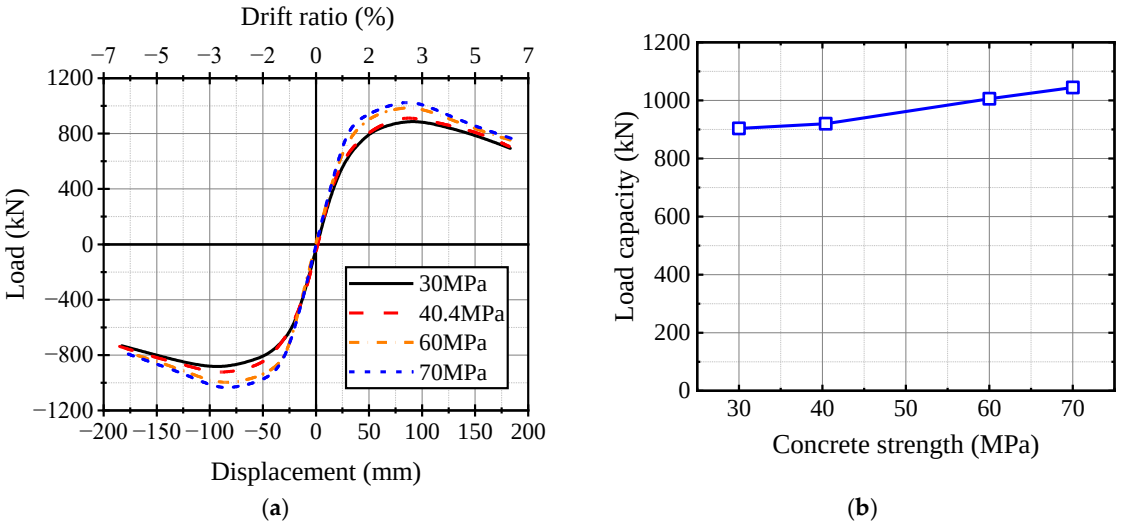


Figure 14. *Cont.*

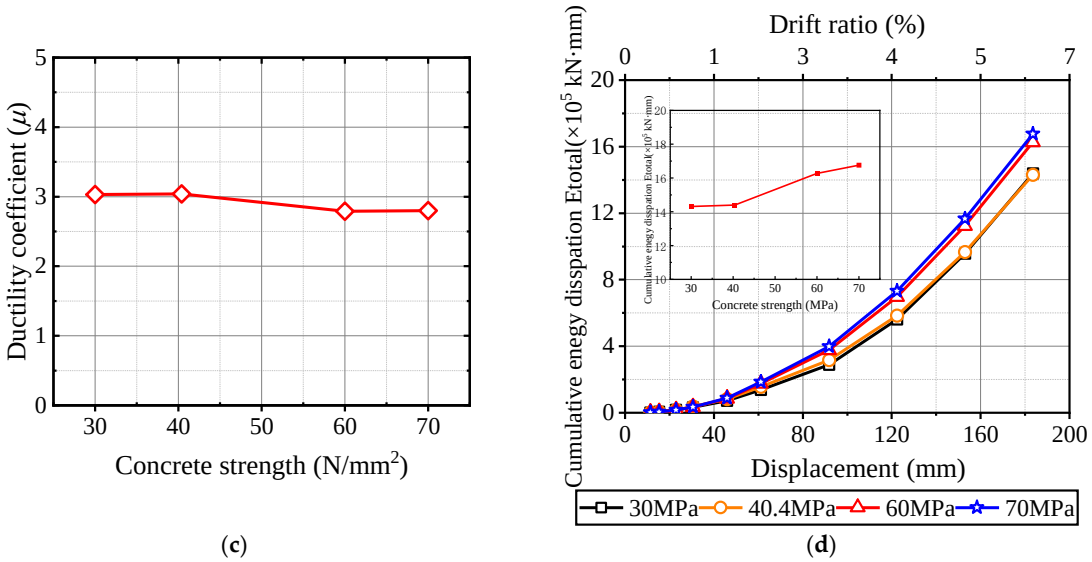
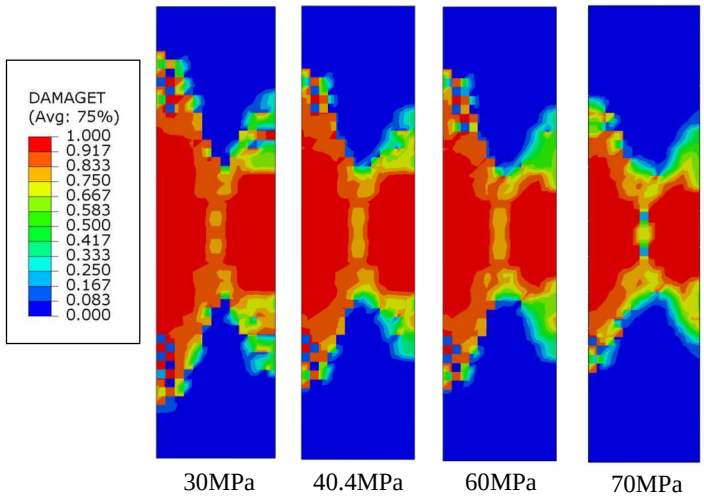
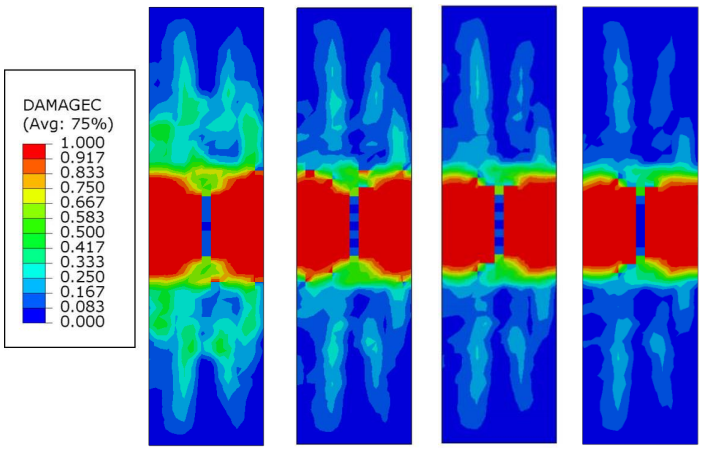


Figure 14. Influence of concrete strength on (**a**) skeleton curves, (**b**) load capacity, (**c**) ductility coefficient, and (**d**) cumulative energy dissipation.



(**a**) Tensile damage status



(**b**) Compressive damage status

Figure 15. (**a**) Tensile and (**b**) compressive damage status at different concrete strength when the story drift reached 6%.

4.3. Effect of Steel Flange Strength

The effect of the steel flange's yield strength was similar to that of the concrete strength. A higher steel flange strength could make the skeleton curve fuller and improve the lateral capacity, as exhibited in Figure 16a,b, as the lateral constraints on the concrete column were strengthened. However, the enlarged stiffness and strength difference between the steel flange strength and the concrete reduced the ductility of the RCS joint. When the yield strength increased from 235 to 460 MPa, the load capacity increased by 25.97% and the ductility coefficient decreased by 17.68%. The steel flange strength did not affect the cumulative energy dissipation when the drift was lower than 4%, but it did make the final energy dissipation increase, as observed in Figure 16d. A yield strength increase from 235 to 460 MPa improved the final energy dissipation by 11.36%. Figure 16e exhibits the highest flange strain development at different flange strengths. Flanges with different yield strengths reached the yield point at a similar drift ratio, namely around 4%. The maximum flange strain decreased with a rise in yield strength, which indicates that high-strength steel flanges can reduce steel beam deformation at failure. The tensile and compressive damage statuses of the concrete column are shown in Figure 17. Both compressive and tensile damages worsened when enhancing the steel flange, since a steel flange with a higher yield strength can exert a higher reactive force on the column under lateral cyclic loading.

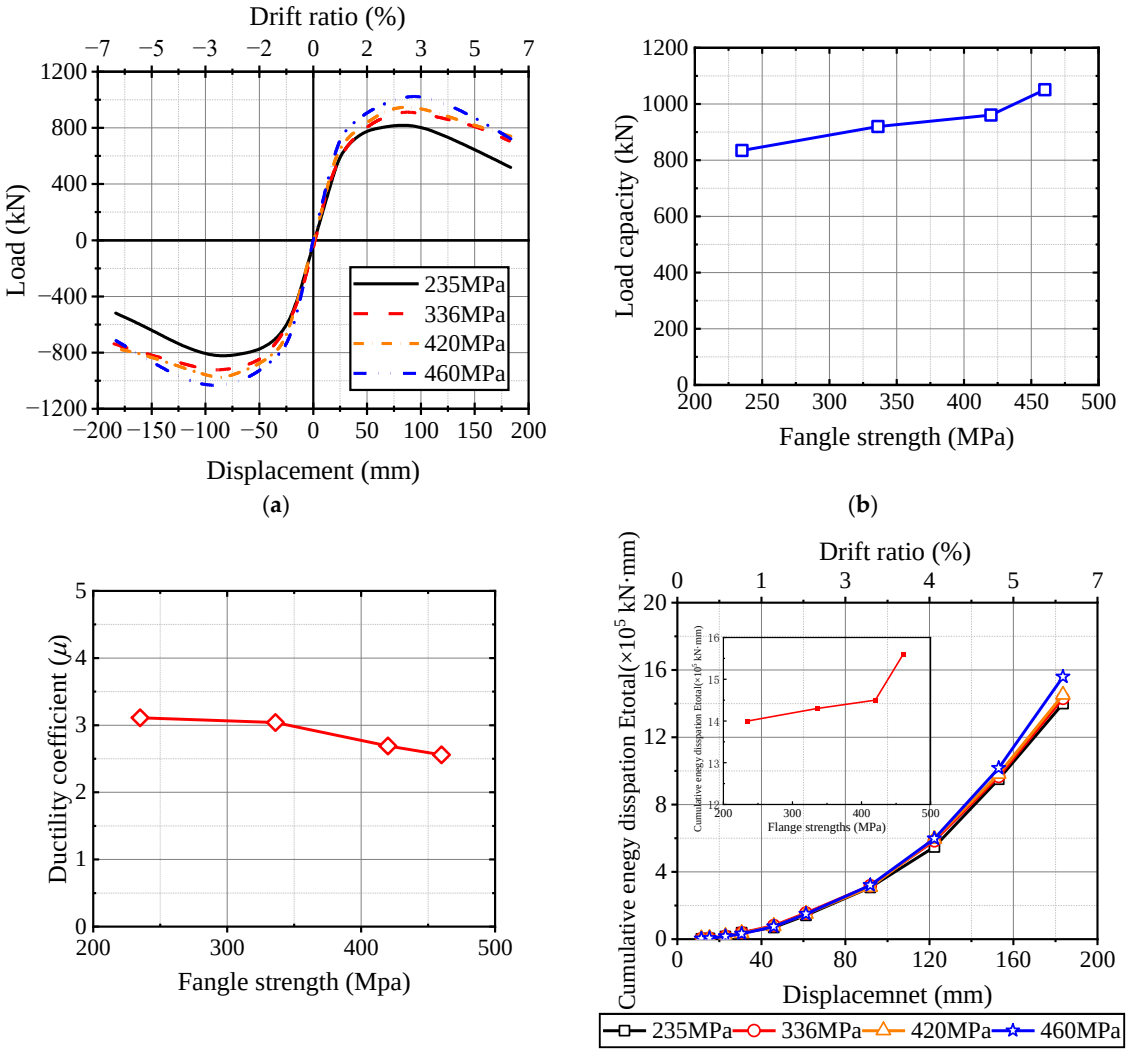
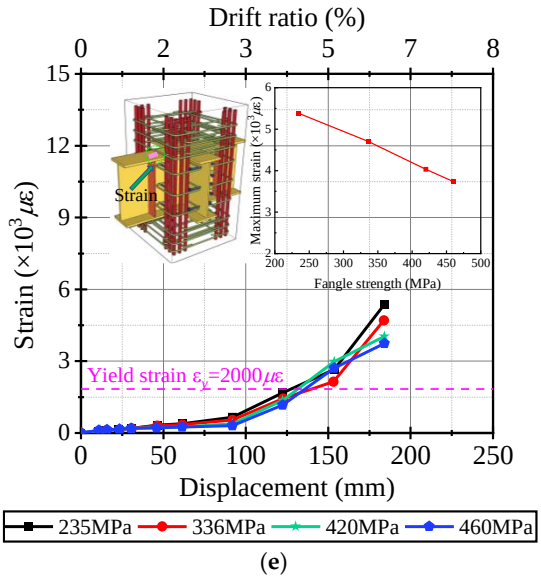
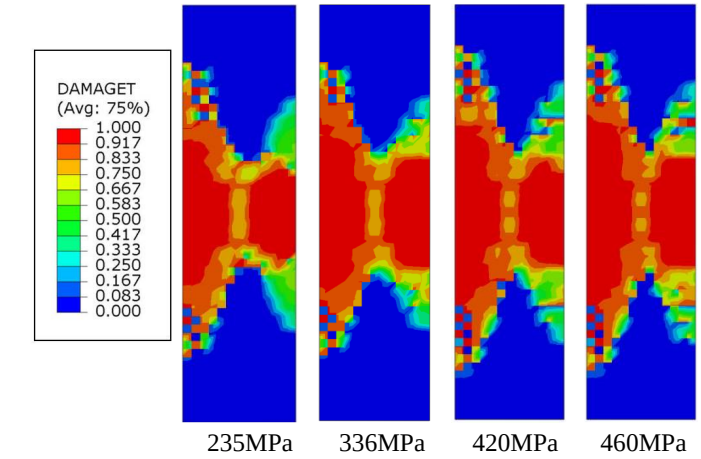


Figure 16. *Cont.*

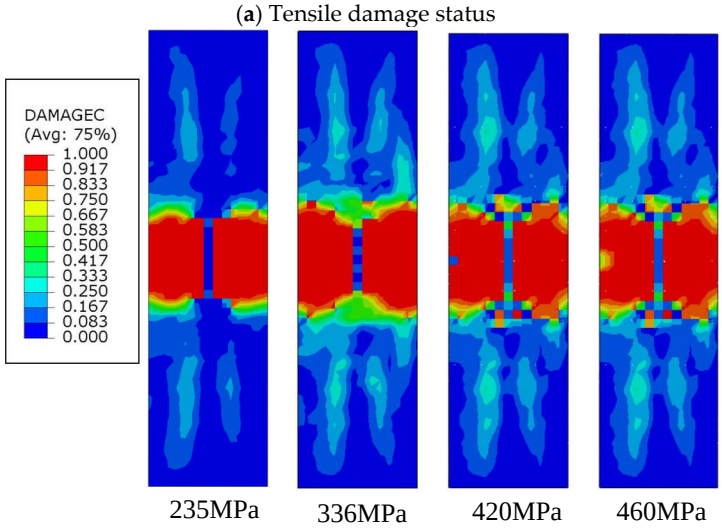


(**e**)

Figure 16. Influence of the steel flange strength on (**a**) skeleton curves, (**b**) load capacity, (**c**) ductility coefficient, (**d**) cumulative energy dissipation, and (**e**) strain on the flange.



(**a**) Tensile damage status

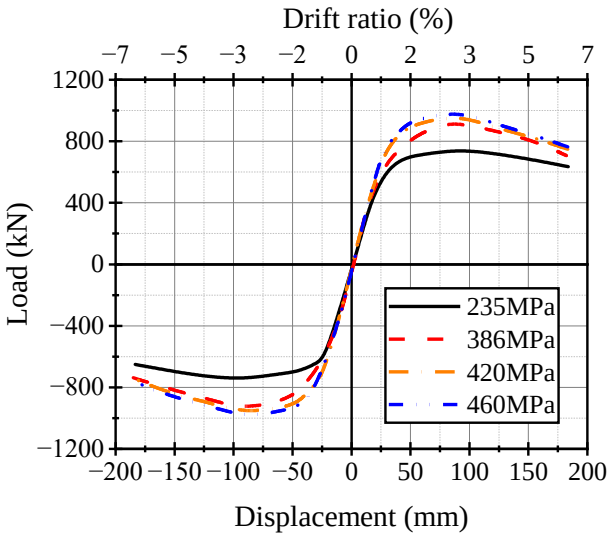


(**b**) Compressive damage status

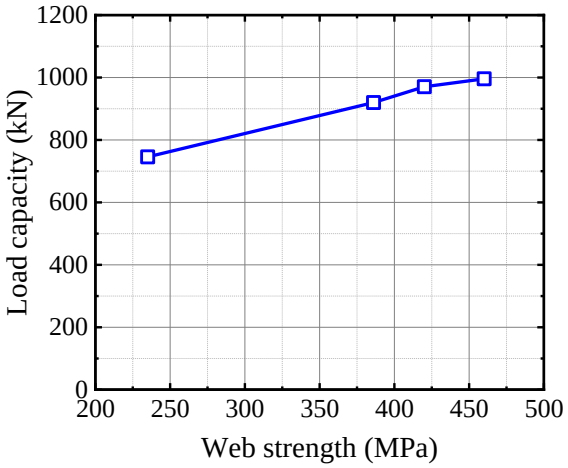
Figure 17. (**a**) Tensile and (**b**) compressive damage status at different steel flange strengths when the story drift was 6%.

4.4. Effect of Steel Web Strength

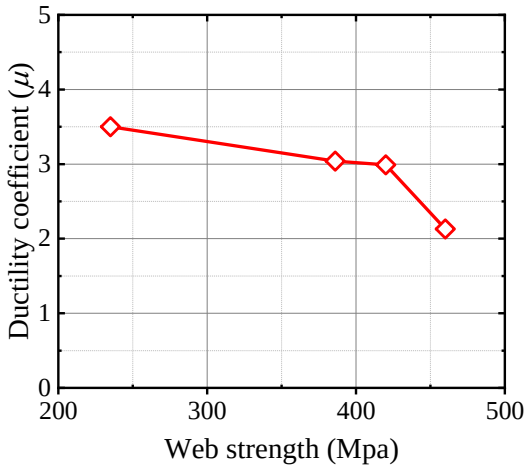
The seismic behavior of RCS joints with various steel web strengths is demonstrated in Figures 18 and 19. Enhancing the steel web had similar influences on the RCS joint performance as strengthening the steel flange. When the web yield strength grew from 235 to 460 MPa, the load capacity and cumulative energy dissipation of the RCS joint were improved by 33.45% and 20.85%, respectively, but the ductility was reduced by 39.14%. The compressive and tensile damage patterns also worsened. Web enhancement exhibited a more significant effect than flange enhancement. In addition, high-strength web utilization could also restrain web deformation and reduce web strain.



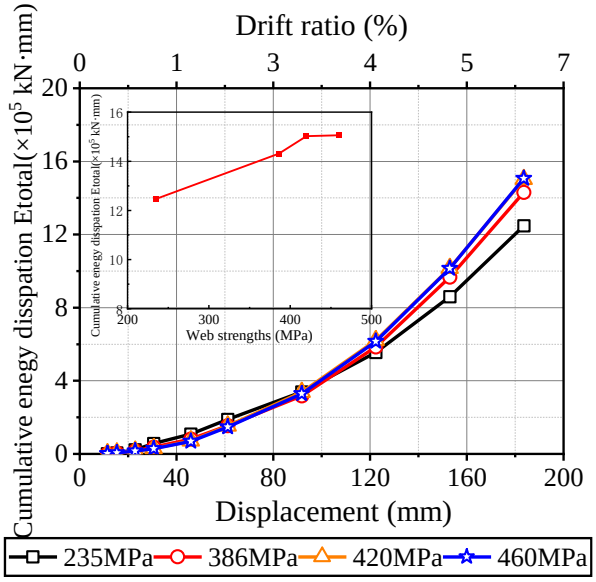
(**a**)



(**b**)

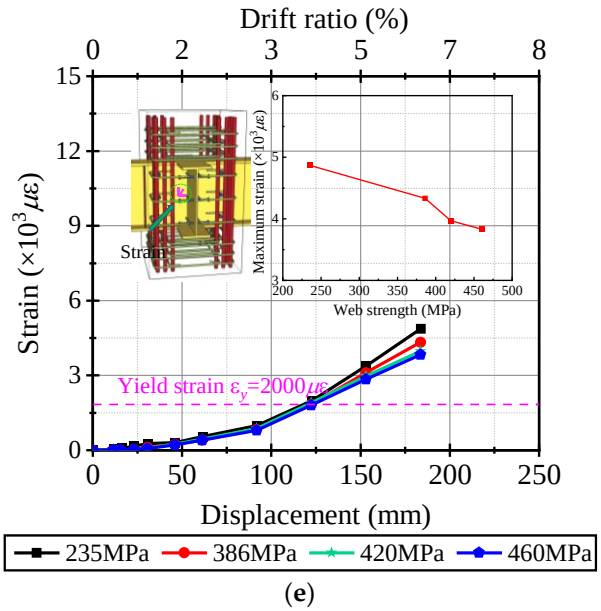


(**c**)



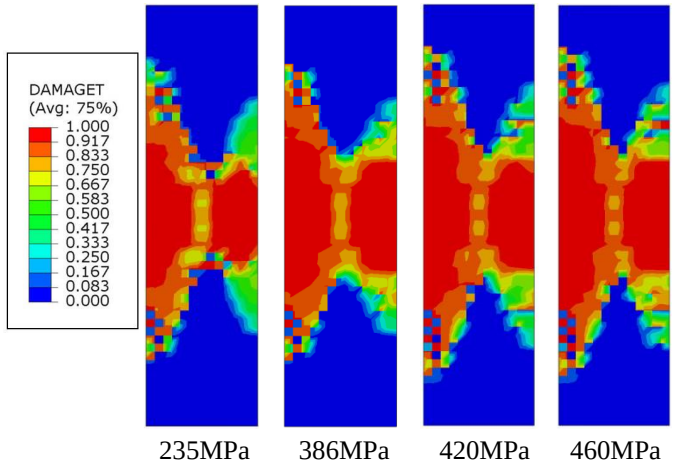
(**d**)

Figure 18. *Cont.*

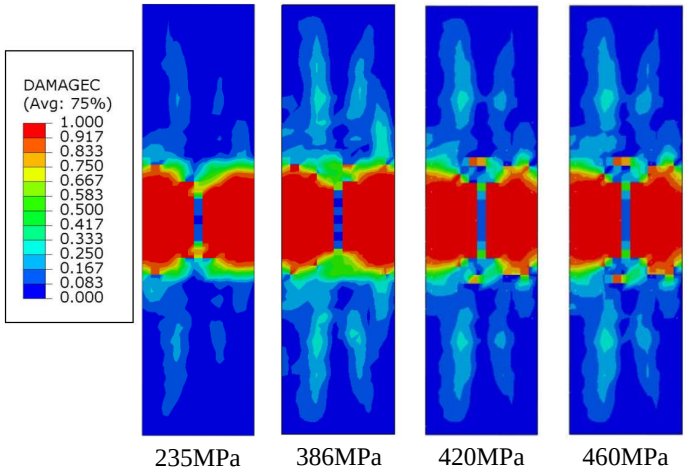


(**e**)

Figure 18. Influence of the steel web strength on (**a**) skeleton curves, (**b**) load capacity, (**c**) ductility coefficient, (**d**) cumulative energy dissipation and (**e**) strain on the web.



(**a**) Tensile damage status



(**b**) Compressive damage status

Figure 19. (**a**) Tensile and (**b**) compressive damage status at different steel web strengths when the story drift was 6%.

4.5. Effect of Transverse Reinforcement Diameter

For most column beam joints, the constraints enforced by the stirrup are the main contributor to the seismic performances of the joint. As observed in Figure 20a, the RCS joint skeleton curves tended to be full with an increase in the reinforcement diameter. Figure 20b–d indicate that the peak capacity, ductility coefficient, and final cumulative energy dissipation were improved by 21.26%, 16.54%, and 25.93%, respectively, when the diameter grew from 4 to 18 mm. The improvements in peak capacity and cumulative energy dissipation were attributed to the stronger constraints caused by transverse reinforcement. The effect of the transverse reinforcement diameter on the ductility was contrasting to that of the concrete and steel strength. An increase in stirrup diameter could restrain the cracking and spalling of the concrete, resulting in a higher RCS joint ductility. The stirrup constraint benefits are also reflected in the concrete compressive and tensile damage status presented in Figure 21. Concrete damage, especially tensile damage, was effectively controlled by using transverse reinforcements with a higher diameter. Additionally, increasing the stirrup diameter could postpone stirrup failure under lateral cyclic loading, as illustrated in Figure 20e. The stirrup with a diameter of 4 mm failed at the drift ratio of 2.5%, while that with a diameter of 18 mm failed at the drift ratio of 4.5%. The maximum stirrup strain increased first and then decreased with an increase in diameter. When the stirrup diameter was low, the stirrup broke before the concrete was crushed, so the final strain increased with the diameter. When the stirrup diameter was over 8 mm, the stirrup was completely used and a smaller strain was sufficient to exhibit the same tensile force, so the final strain decreased with the diameter.

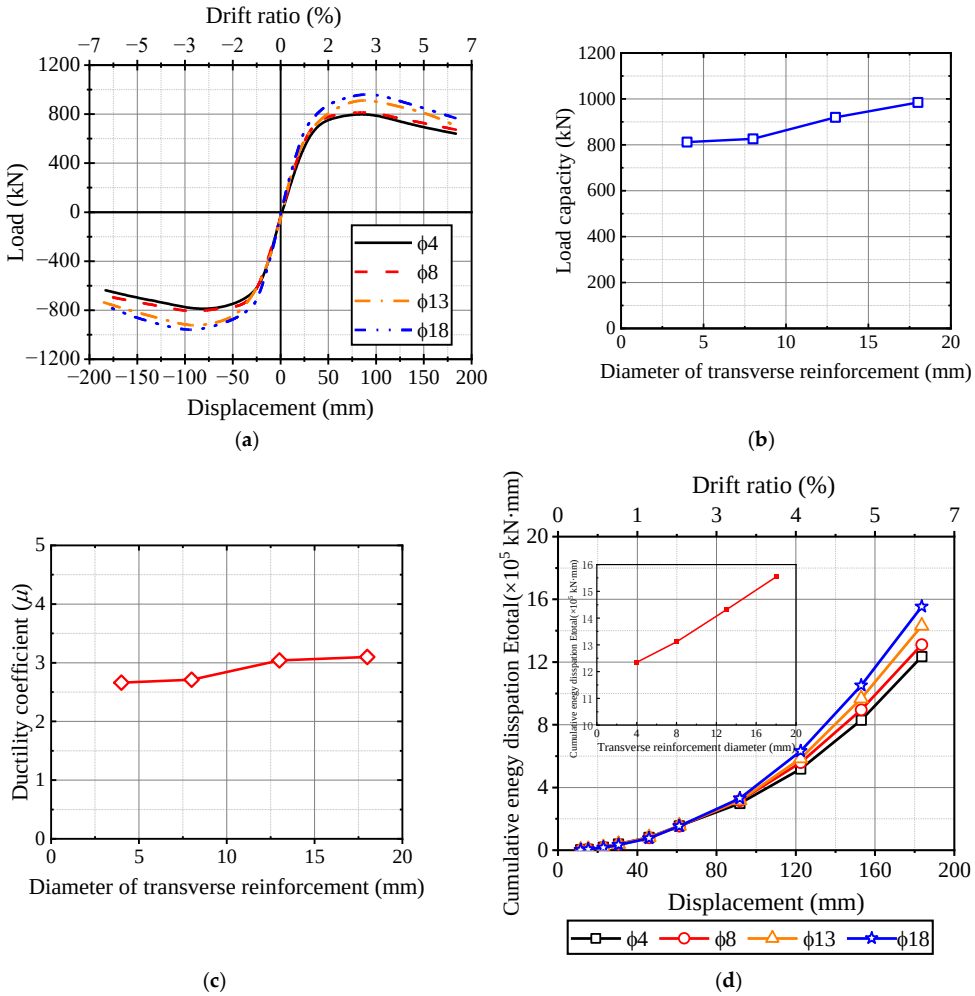
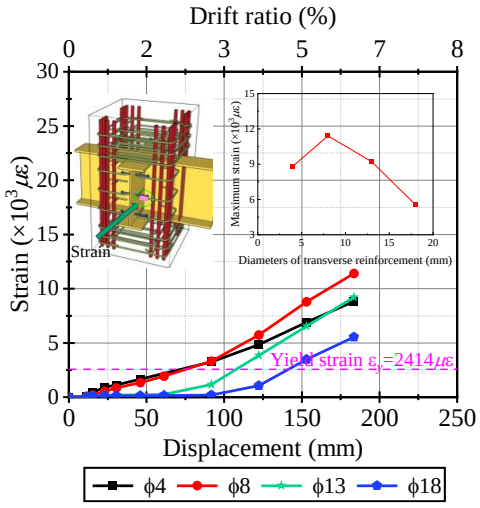
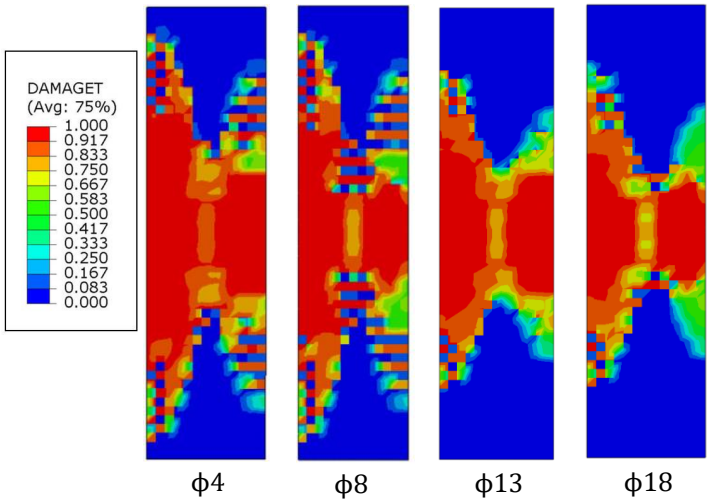


Figure 20. *Cont.*

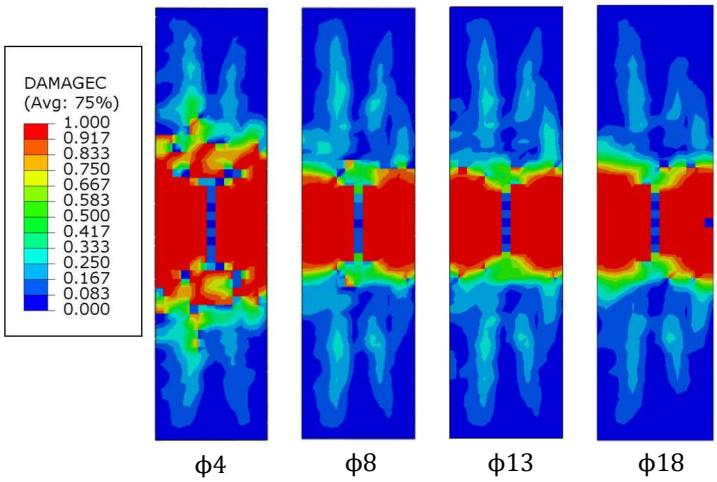


(**e**)

Figure 20. Influence of the transverse reinforcement diameter on (**a**) skeleton curves, (**b**) load capacity, (**c**) ductility coefficient, (**d**) cumulative energy dissipation, and (**e**) strain on transverse reinforcement.



(**a**) Tensile damage status



(**b**) Compressive damage status

Figure 21. (**a**) Tensile and (**b**) compressive damage status at different transverse reinforcement diameters when the story drift was 6%.

4.6. Effect of Longitudinal Reinforcement Diameter

As demonstrated in Figure 22a, the skeleton curves of the RCS joints were dramatically modified by varying the longitudinal reinforcement diameter. It can be observed in Figure 22b,d that both the peak load and the energy dissipation were enhanced by 80.38% and 71.37%, respectively, when the diameter increased from 12 to 29 mm, since a larger diameter enables the reinforcement to resist a higher load and dissipate more energy. As noted in Figure 22e, an increase in the longitudinal bar diameter could also postpone rebar failure. A reinforcement bar with a small diameter, i.e., 12 mm, breaks before the concrete is crushed, which adversely influences RCS joint ductility. When the rebar diameter was large, i.e., 29 mm, the steel bar could not yield or sufficiently deform, which also worsened the ductility. Therefore, the ductility coefficient exhibited a tendency to increase and then decrease with an increase in rebar diameter, as highlighted in Figure 22c. In addition, the longitudinal bar could effectively control horizontal tensile crack development, which mitigated the tensile damage, as demonstrated in Figure 23a. Since the compressive load was mainly sustained by the concrete, the change in the longitudinal bar diameter had little influence on the compressive damage status, as shown in Figure 23b.

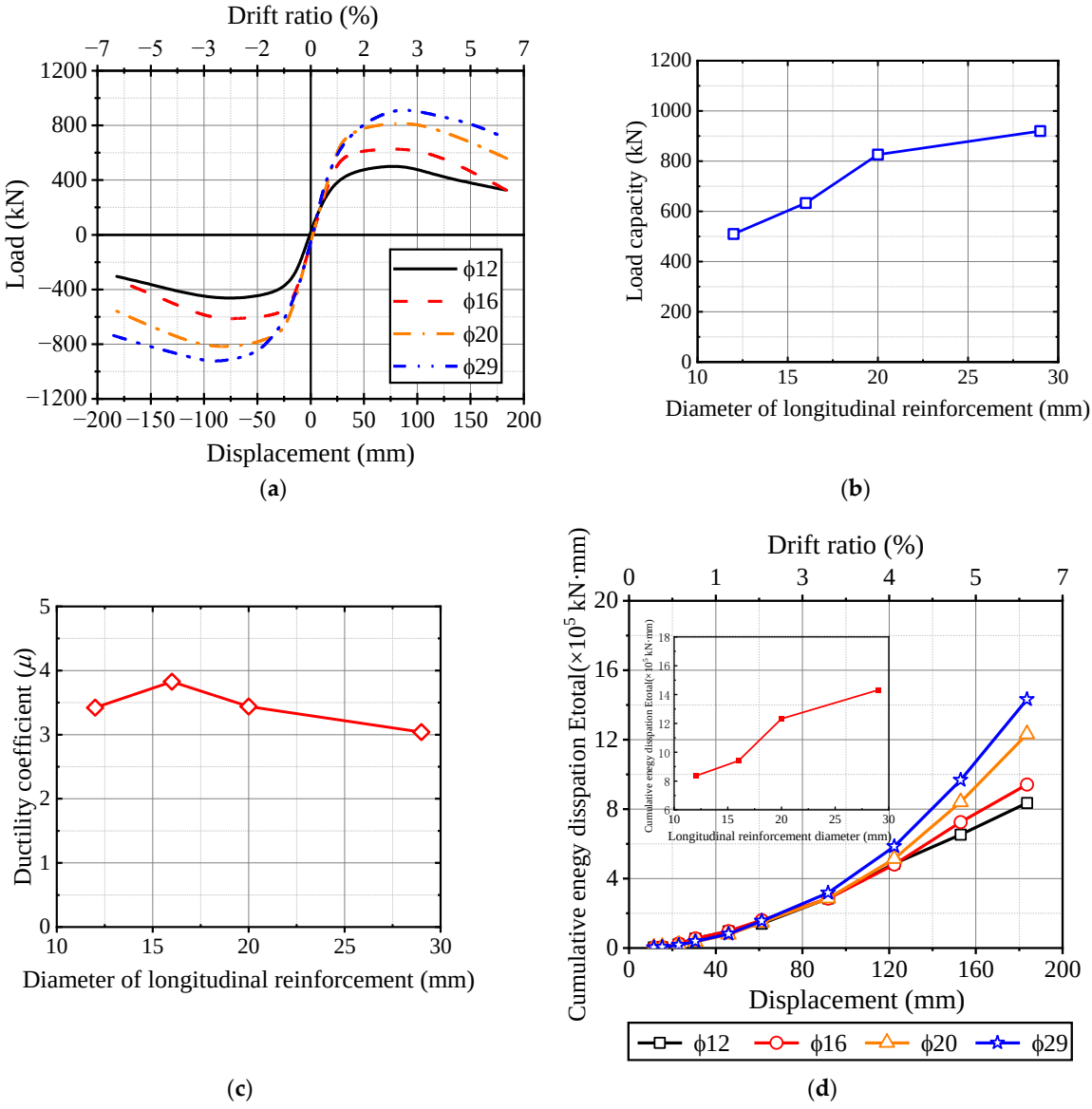
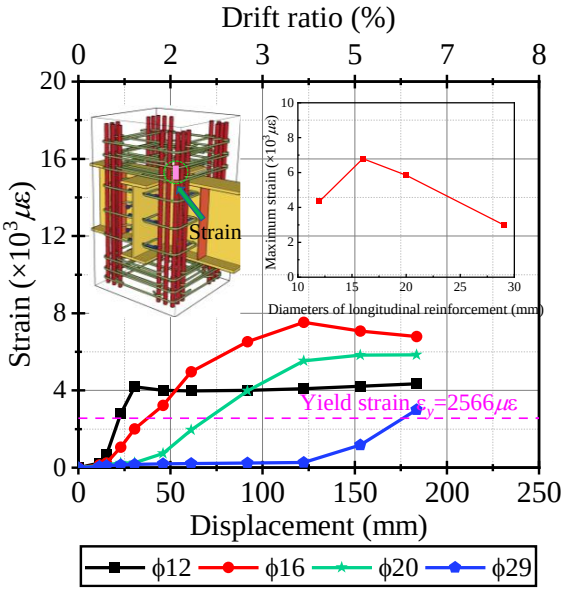
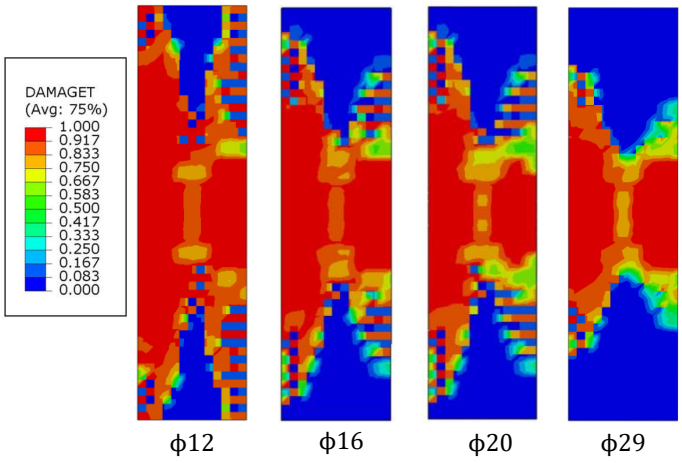


Figure 22. *Cont.*

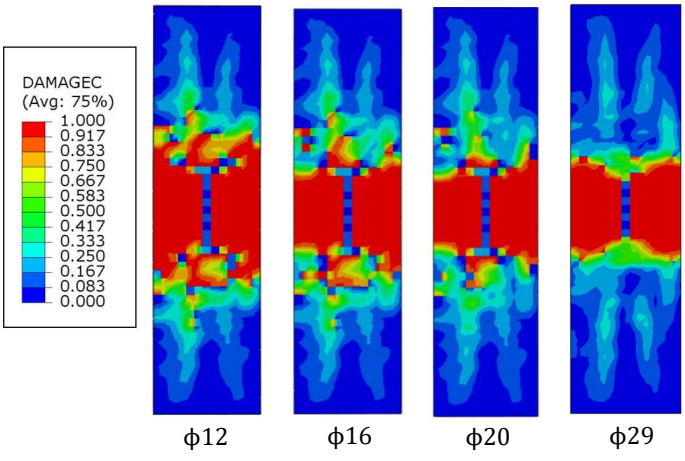


(**e**)

Figure 22. Influence of the longitudinal reinforcement diameter on (**a**) skeleton curves, (**b**) load capacity, (**c**) ductility coefficient, (**d**) cumulative energy dissipation, and (**e**) strain on longitudinal reinforcement.



(**a**) Tensile damage status



(**b**) Compressive damage status

Figure 23. (**a**) Tensile and (**b**) compressive damage status at different longitudinal reinforcement diameters when the story drift was 6%.

5. Theoretical Capacity Estimation

Six commonly used capacity evaluation methods were employed to theoretically estimate the RCS joint capacity. Three of them, namely ASCE [31], CECS [32], and AIJ [33], were introduced by the national codes of USA, China, and Japan, while the others, namely Kanno [34], Modified-Kanno [35], and Nishiyama et al. [36], were proposed by researchers. These six methods are listed and detailed in Table 4. The calculated and simulated values obtained under different evaluation methods for specimens with different parameters are shown in Figure 24, and the average relative error is shown in Figure 25. The average value and average relative error of the ratio of the two were consistent. The ASCE, Kanno, and M-Kanno methods estimated more conservative bearing capacity evaluation values, as they did not consider the strengthening effects of transverse beams and other reinforcing elements, resulting in negative average relative errors. The calculation method provided by CECS additionally considered the strengthening effect of the web, resulting in its calculated value being much larger than the simulated value with an average relative error exceeding 50%. Through an analysis of evaluation indicators such as average value, standard deviation, coefficient of variation, and average relative error, the modified M-Kanno method had the highest accuracy in bearing capacity evaluation and is suitable for seismic bearing capacity evaluations of this simple structural RCS joint.

Table 4. Theoretical capacity evaluation methods for RCS joints.

No.	Capacity Evaluation Method	Equation
1	USA Code: ASCE [31]	$V_c = \frac{\left[V_s d_f + 0.75 V_n d_w + V_n'(d+d_o)\right]}{\left(L_c - d - \frac{L_c}{L_b} jh\right)}$ where $V_s = 0.6 F_{yw} t_w jh,\ V_n = 1.7\sqrt{f_c'} b_p h \le 0.5 f_c' b_p d_w$, $V_n' = V_c' + V_s' = 0.4\sqrt{f_c'} b_o h + A_{sh} F_{ysh} 0.9h/s_h \le 1.7\sqrt{f_c'} b_o h$
2	Chinese Code: CECS [32]	$V_c = \frac{L_b(d-t_f)}{L_b(L_c-d+t_f)-bL_c}\left[\frac{1}{\gamma_{RE}} 0.14 \alpha bh f_c + 0.58 t_w d_w F_{yw}\right]$
3	Japanese Code: AIJ [33]	$V_c = \frac{L_b(d-t_f)}{L_b(L_c-d+t_f)-bL_c}\left[\frac{k_w \cdot t_w \cdot h \cdot F_{yw}}{\sqrt{3}} + 0.25 p_w \cdot F_{ysh} \cdot b \cdot {}_m d + {}_c k_1 \cdot {}_c k_2 \cdot 0.4b \cdot h \cdot 0.3 f_c'\right]$
4	Kanno [34]	$V_c = \frac{L_b}{L_c} \cdot \frac{0.9d}{L_b - h}\left(V_s + V_{sf} + V_n + V_n'\right)$ where $V_s = t_w \frac{F_{yw}}{\sqrt{3}} jh,\ V_{sf} = \frac{4M_{pf}}{d_f},\ M_{pf} = \frac{t_f^2}{4} F_{yf} b_f,\ V_n = 1.65\sqrt{f_c'} b_p h$, $V_n' = V_c' + V_s' = 1.05\sqrt{f_c'} b_o h + \frac{A_{sh} F_{ysh} 0.9h}{s_h}$
5	Modified-Kanno (M-Kanno) [35]	$V_c = \frac{V_s d_f + 0.75 V_n d_w + V_n' d_j}{(L_c - d_j)}$ where $V_s = \left(\frac{F_{yw}}{\sqrt{3}}\right) t_w jh,\ V_n = 1.65\sqrt{f_c'} b_i h$, $V_n' = V_c' + V_s' = 1.05\sqrt{f_c'} b_i h + \left(A_{sh} F_{ysh} 0.9h\right)/s_h$
6	Nishiyama et al. [36]	$V_c = \frac{L_b(d-t_f)}{L_b(L_c-d+t_f)-bL_c}[V_s + V_s' + V_c']$ where $V_s = C_1 t_w d_w F_{yw}/\sqrt{3}$, $V_s' = 0.25 p_w F_{ysh}/\sqrt{3}$, $V_c' = 0.04 C_2 C_3 bh f_c \cdot J\delta$

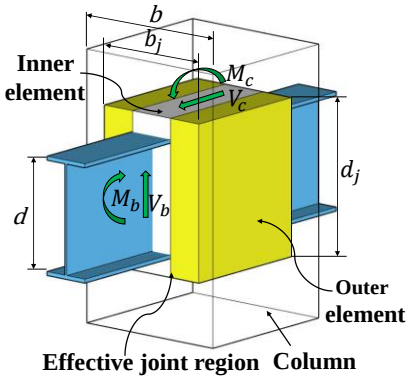
Table 4. *Cont.*

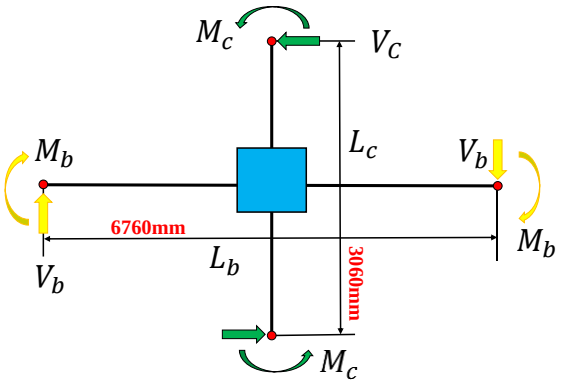
No.	Capacity Evaluation Method	Equation

Symbols:

V_s: horizontal shear force in the steel panel
V_s': shear strength of transverse reinforcement
V_n: internal concrete shear strength
V_n': external shear strength
V_{sf}: flange shear strength
V_c': external concrete shear strength
L_c: vertical calculation length of beam
L_b: horizontal calculation length of the column
d_w: height of the web
d_f: distance between beam flange centerlines
d_j: effective connection height
d: depth of the steel beam
t_f: thickness of beam flanges
t_w: thickness of the beam web
b_o: effective width of the outer concrete panel
b_p: width of the FBP
b_f: width of the flange
b_i: width of the inner concrete panel
F_{yw}: yield strength of the beam web
F_{yf}: yield strength of the beam flange
F_{ysh}: yield strength of column ties
p_w: transverse reinforcement ratio
$J\delta$: shape factor of beam-column joints
jh: effective width of the beam web
f_c': characteristic compressive strength of concrete
M_{pf}: full plastic moment of the steel beam
f_c: design value of concrete compressive strength
s_h: center-to-center spacing of stirrup
A_{sh}: cross-sectional area of the reinforcement parallel to the beam
d_o: additional effective joint depth provided by attachments to beam flanges
${}_md$: maximum distance between tensile and compressive steel bars
α: influence coefficient of joint position (1.0 for the middle joint)
k_w: joint effective coefficient (0.9 for the case without cover plates)
C_1: joint construction factor (0.9 for the case with an FBP)
C_2 : joint construction factor (1.0 for the case with an FBP)
C_3 : joint construction factor (1.0 for the case with a transverse beam)
${}_ck_1$: joint enhancement coefficient (1.0 for the base case)
${}_ck_2$: joint enhancement coefficient (1.0 for the case with the transverse beam going through the column)
b: width of concrete column measured perpendicular to the beam
h: depth of concrete column measured parallel to the beam
γ_{RE}: seismic capacity adjustment coefficient, 0.85

Schematical diagram:





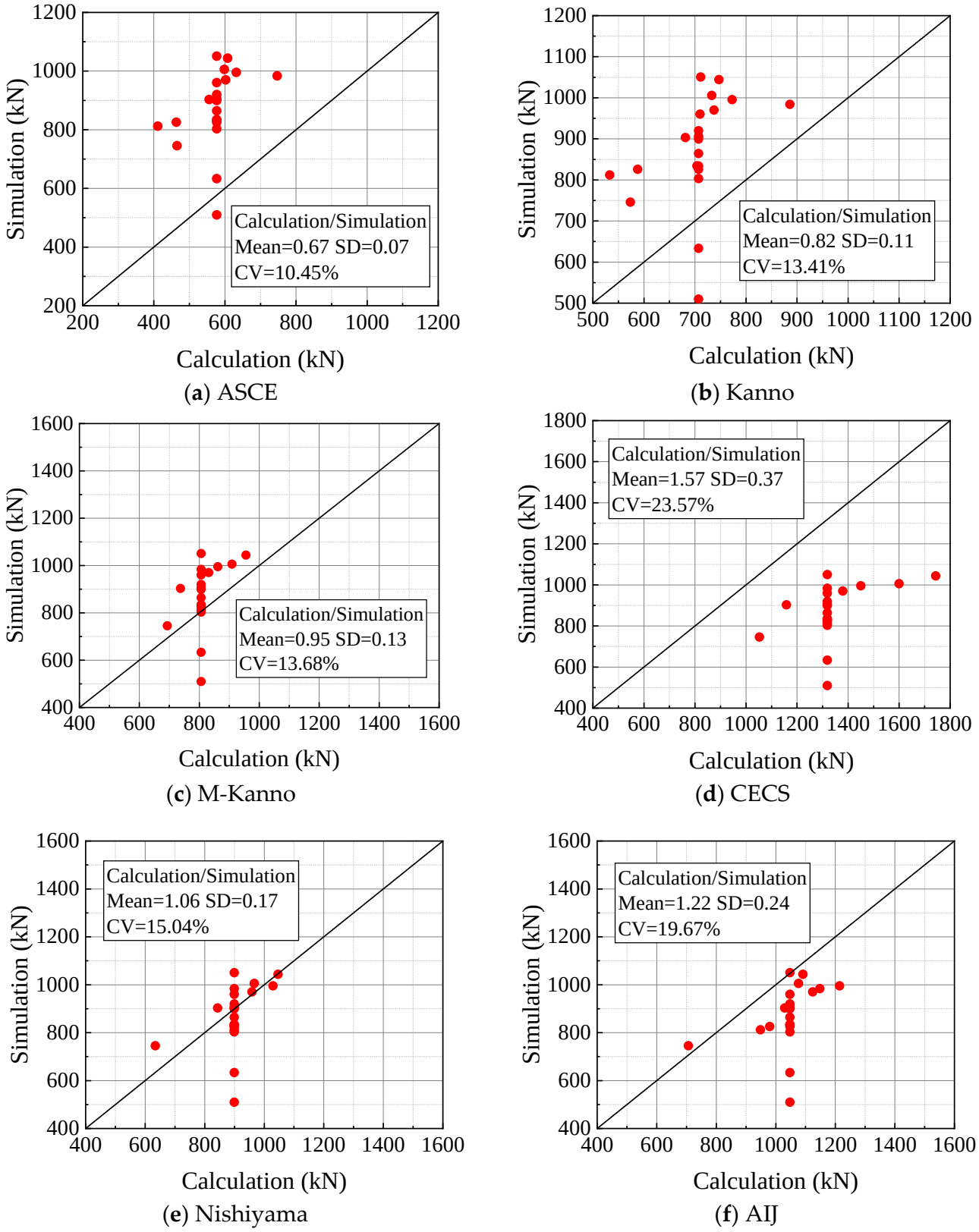


Figure 24. Shear capacity comparison between the calculated and simulated results of the six evaluation methods.

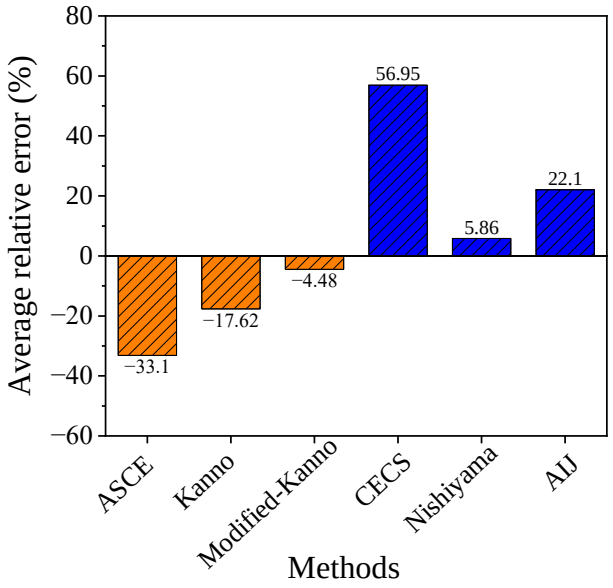


Figure 25. Error of the theoretical capacity evaluation methods for the RCS joint.

6. Conclusions

A finite element analysis (FEA) model, validated by the experimental data, was adopted to numerically investigate the seismic performance of simply configured reinforced concrete column–steel beam (RCS) joints and determine a theoretical evaluation equation. The following conclusions were drawn:

(1) The comparison between finite element analysis and experimental results indicated that the finite element model could accurately reproduce the hysteresis characteristics and cracking modes of simplified RCS joints under earthquake conditions. The experimental and numerical results were used as the basis for a theoretical analysis, providing a theoretical basis for the subsequent seismic design of simplified RCS joints.

(2) An increase in the axial compression ratio enhanced the vertical constraint effect, suppressed tensile crack development, and improved the bearing capacity of concrete columns. At the same time, the deformation capacity was constrained, resulting in a significant decrease in ductility and energy consumption. When the axial compression ratio was 30%, the overall seismic performance of the specimen was good. However, when the axial compression ratio exceeded 30%, the increase in bearing capacity was limited, while the ductility and energy consumption were significantly reduced, which had a negative impact on seismic performance. High-strength concrete utilization can improve the load capacity and energy dissipation in RCS joints and reduce concrete damage, although the ductility will be adversely affected.

(3) The use of high-strength concrete could significantly improve the bearing capacity and energy consumption of simplified RCS joints and reduce concrete damage. The bearing capacity and energy consumption increased by 15.6% and 16.39%, respectively.

(4) Increases in web and flange steel strengths could strengthen the energy dissipation and load capacity under cyclic loads, but they reduced the ductility and aggravated concrete damage. When the yield strength exceeded 420 MPa, the concrete damage reached its limit, and crack propagation was no longer significant. The load capacity, energy dissipation, and concrete damage pattern could be effectively improved by increasing the diameters of either the longitudinal or transverse reinforcements. Utilizing a stirrup with a larger diameter is a good way to increase joint ductility.

(5) By increasing longitudinal or transverse steel bar diameters, the steel bar restraining effect on concrete was enhanced, effectively improving the bearing capacity, energy dissipation, and concrete damage mode. Using a larger diameter stirrup was a good method to improve the joint's ductility. However, from the perspective of strain

development, the deformation capacity of larger steel bars was constrained and the strain increase was slower, resulting in a decrease in the ductility of the specimen.

(6) In a comparison of various bearing capacity calculation methods, it was found that the calculation methods provided by ASCE, Kanno, and M-Kanno were relatively conservative due to the lack of consideration of the influence of transverse beams. The formula provided by CECS takes into account the additional strengthening effect of the web, and its calculated value was much greater than the simulated value. Through a comparative analysis, the modified calculation method proposed by Kanno showed a relative bearing capacity error of less than 5%, demonstrating it could better predict the bearing capacity of simplified RCS joints.

Author Contributions: Conceptualization, W.L.; Methodology, W.L., L.C., Z.W. and B.C.; Software, Z.W., W.L. and X.L.; Validation, Z.W. and B.C.; Resources, W.L. and L.C.; Writing—original draft, Z.W. and W.L.; Writing—review and editing, W.L. and Z.W.; Supervision, W.L., L.C. and B.C.; Project administration, L.C. and W.L. All authors have read and agreed to the published version of the manuscript.

Funding: Construction scientific research project of Department of Housing and Urban-Rural Development of Zhejiang Province (No. 2022K245), National Natural Science Foundation of China (NSFC) (Nos. 51308419 and 51578422), Zhejiang Province Public Welfare Technology Application Research Project (No. LGF22E080004), and Wenzhou Association for Science and Technology (No. kjfw34).

Informed Consent Statement: Not applicable.

Data Availability Statement: Not applicable.

Conflicts of Interest: The authors declare no conflict of interest.

References

1. Benavent-Climent, A.; Cahís, X.; Zahran, R. Exterior wide beam–column connections in existing RC frames subjected to lateral earthquake loads. *Eng. Struct.* **2009**, *31*, 1414–1424. [CrossRef]
2. Masi, A.; Santarsiero, G.; Nigro, D. Cyclic tests on external RC beam-column joints: Role of seismic design level and axial load value on the ultimate capacity. *J. Earthq. Eng.* **2013**, *17*, 110–136. [CrossRef]
3. Zhao, Z.Z.; Qian, J.R.; Yang, X.B.; Zhu, W.Y. Experimental Study on Behavior of Reinforced Concrete Column-steel Beam Subassemblies. *Build. Struct.* **2006**, *8*, 69–73.
4. Guo, Z.X.; Zhu, Q.Y.; Liu, Y.; Huang, Q.X. Experimental study on seismic behavior of a new type of prefabricated RC column-steel beam frame connections. *J. Build. Struct.* **2012**, *33*, 69–73.
5. Li, Z.H.; Peng, Z.H.; Qi, Y.H.; Teng, J.; Ou, J.P. Full-scale experimental study on seismic behaviors of plasticity controllable steel joint of prefabricated RC beam column. *J. Build. Struct.* **2019**, *40*, 43–50.
6. Guo, Z.P.; Zhou, C.; Li, L.M. Research on Seismic Behavior of Composite Joint of Prefabricated Reinforced Concrete Column-steel Beam. *Constr. Technol.* **2020**, *49*, 19–22+51.
7. Ghods, S.; Kheyroddin, A.; Nazeryan, M.; Mirtaheri, M.; Gholhaki, M. Nonlinear behavior of connections in RCS frames with bracing and steel plate shear wall. *Steel Compos. Struct.* **2016**, *22*, 915–935. [CrossRef]
8. Eghbali, N.B.; Mirghaderi, S.R. Experimental investigation of steel beam to RC column connection via a through-plate. *J. Constr. Steel Res.* **2017**, *133*, 125–140. [CrossRef]
9. Azar, B.F.; Ghaffarzadeh, H.; Talebian, N. Seismic performance of composite RCS special moment frames. *KSCE J. Civ. Eng.* **2013**, *17*, 450–457. [CrossRef]
10. Karande, P.; Shiyekar, M.; Ghugal, Y. Study of the behaviour of RC and RCS frame. *Int. J. Eng. Sci. Res. Technol.* **2020**, *9*, 2277–9655.
11. Nabati, M.; Zirakian, T.; Shahmohammadi, A.; Hajsadeghi, M. Structural Performance Assessment of Through-Column-Type Beam-to-Column Joints. *Am. J. Civ. Eng. Archit.* **2018**, *6*, 158–167. [CrossRef]
12. Le, D.D.; Nguyen, X.H.; Nguyen, Q.H. Cyclic Testing of a Composite Joint between a Reinforced Concrete Column and a Steel Beam. *Appl. Sci.* **2020**, *10*, 2385.
13. Herdiansah, Y.; Budiono, B.; Soemari, H.D.; Sidi, I.D. Behavior of RCS Connections with Void Web Under Cyclic Load Reversals. *J. Eng. Sci. Technol.* **2020**, *52*, 837–854. [CrossRef]
14. Doost, R.B.; Khaloo, A. Steel web panel influence on seismic behavior of proposed precast RCS connections. *Structures* **2021**, *32*, 87–95. [CrossRef]
15. Chen, H.; Guo, Z.X.; Basha, S.H.; Liu, Y. Seismic behavior of RCS frame joints applied with high-strength bolts-end plate connection. *J. Build. Eng.* **2023**, *63*, 105455. [CrossRef]
16. Cheng, C.T.; Chen, C.C. Seismic behavior of steel beam and reinforced concrete column connections. *J. Constr. Steel Res.* **2015**, *61*, 587–606. [CrossRef]

17. Nguyen, X.H.; Le, D.D.; Nguyen, Q.H.; Nguyen, H.Q. Seismic performance of RCS beam-column joints using fiber reinforced concrete. *Earthq. Struct.* **2020**, *18*, 599–607.
18. Li, W.; Li, Q.N.; Jiang, W.S. Parameter study on composite frames consisting of steel beams and reinforced concrete columns. *J. Constr. Steel Res.* **2012**, *77*, 145–162. [CrossRef]
19. Naserifard, M.; Vetr, M.G. Parametric study on behavior of steel beam to reinforced concrete column connections in moment frames. *Int. J. Steel Struct.* **2019**, *19*, 1511–1520. [CrossRef]
20. Ling, Y.H.; Xu, J.H.; Guo, Z.H.; Wen, X.G. A study on Static behavior of New Reinforced concrete column-steel beam Composite Joints. *J. Asian Archit. Build. Eng.* **2021**, *20*, 44–60. [CrossRef]
21. Alizadeh, S.; Attari, N.K.A.; Kazemi, M.T. The seismic performance of new detailing for RCS connections. *J. Constr. Steel Res.* **2013**, *91*, 76–88. [CrossRef]
22. Jafari, R.; Attari, N.K.A.; Nikkhoo, A.; Alozadeh, S. Simplified method for modeling reinforced concrete column-steel beam connections with tube plate. *Adv. Struct. Eng.* **2020**, *23*, 2292–2304. [CrossRef]
23. Li, W.; Ye, H.; Liu, H.J.; Chen, B.X. Development and experimenting of demountable RC column-to-steel beam connections under cyclic loading. *Soil Dyn. Earthq. Eng.* **2022**, *159*, 107342. [CrossRef]
24. Li, W.; Ye, H.; Wang, Q.; Liu, H.J.; Ding, T.; Liu, B. Experimental study on the seismic performance of demountable RCS joints. *J. Build. Eng.* **2022**, *49*, 104082. [CrossRef]
25. Lee, H.J.; Park, H.G.; Hwang, H.J.; Kim, C.S. Cyclic Lateral Load Test for RC Column-Steel Beam Joints with Simplified Connection Details. *J. Struct. Eng.* **2019**, *145*, 04019075.1–04019075.12. [CrossRef]
26. AISC. *Seismic Provisions for Structural Steel Buildings*; ANSI/AISC 341; AISC: Chicago, IL, USA, 2010.
27. *GB 50010-2010*; Ministry of Construction of the People's Republic of China. Code for Design of Concrete Structures. China Architecture Publishing: Beijing, China, 2010.
28. Liu, W. Research on the Working Mechanism of Concrete Filled Steel Tube under Local Compression. Doctoral Dissertation, Fuzhou University, Fuzhou, China, 2005.
29. Khaloo, A.; Doost, R.B. Seismic performance of precast RC column to steel beam connections with variable joint configurations. *Eng. Struct.* **2018**, *160*, 408–418. [CrossRef]
30. Pauletta, M.; Di Marco, C.; Frappa, G.; Somma, G.; Pitacco, I.; Miani, M.; Das, S.; Russo, G. Semi-empirical model for shear strength of RC interior beam-column joints subjected to cyclic loads. *Eng. Struct.* **2020**, *224*, 111223. [CrossRef]
31. ASCE Task Committee on Design Criteria for Composite Structures in Steel and Concrete. Guidelines for design of joints between steel beams and reinforced concrete columns. *J. Struct. Eng.* **1994**, *120*, 2330–2357. [CrossRef]
32. China Association for Engineering Construction. *Technical Specification for Frame Structure of Confined RC Columns and Composite Beams*; CECS 347: 2013; China Architecture and Building Press: Beijing, China, 2013.
33. Architectural Institute of Japan. *Stress Transferring Mechanism and Resistance Mechanism of Steel-Reinforced*; Architectural Institute of Japan: Tokyo, Japan, 2011.
34. Kanno, R. Strength, Deformation, and Seismic Resistance of Joints between Steel Beams and Reinforced Concrete Columns. Ph.D. Thesis, Cornell University, Ithaca, NY, USA, 1993. Volumes I and II.
35. Kanno, R. Evaluation of existing strength models for RCS joints and consideration toward improved modeling: A study on strength evaluation of RCS joints part 1. *J. Struct. Constr. Eng.* **2002**, *553*, 135–142. [CrossRef]
36. Nishiyama, I.; Kuramoto, H.; Noguchi, H. Guidelines: Seismic design of composite reinforced concrete and steel buildings. *J. Struct. Eng.* **2004**, *130*, 336–342. [CrossRef]

Disclaimer/Publisher's Note: The statements, opinions and data contained in all publications are solely those of the individual author(s) and contributor(s) and not of MDPI and/or the editor(s). MDPI and/or the editor(s) disclaim responsibility for any injury to people or property resulting from any ideas, methods, instructions or products referred to in the content.